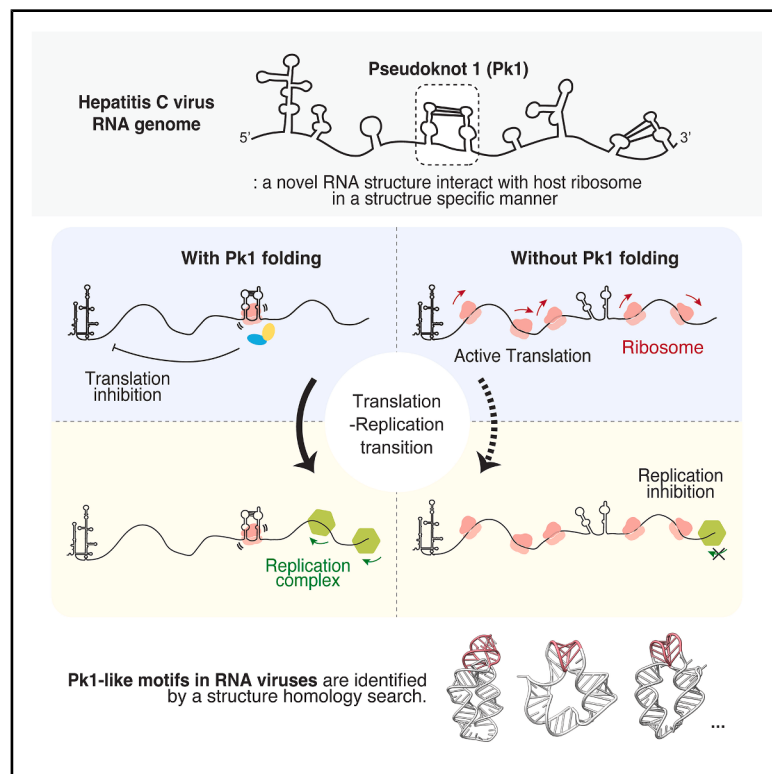


A ribosome-bound pseudoknot in the HCV coding region stimulates viral growth by tuning viral translation

Graphical abstract



Authors

Han Wan, Harim Jang, Ling Xu,
Kyrillos S. Abdallah, Wendy V. Gilbert,
Anna Marie Pyle

Correspondence

anna.pyle@yale.edu

In brief

Wan et al. identified a compact pseudoknot structure (pk1) within the HCV ORF that suppresses the translation of viral proteins. Pk1 interacts with host ribosomes in a structure-specific manner, inhibiting upstream and downstream translation. This may help the virus switch from active translation to replication.

Highlights

- HCV pseudoknot1 forms a compact structure that binds the host ribosome
- Pk1 inhibits upstream and downstream protein translation efficiency
- Pk1 helps rebalance HCV RNA from active translation to RNA replication
- Structure homology search reveals pk1-like structures across viral families



Article

A ribosome-bound pseudoknot in the HCV coding region stimulates viral growth by tuning viral translation

Han Wan,¹ Harim Jang,^{1,4} Ling Xu,^{1,4} Kyrillos S. Abdallah,² Wendy V. Gilbert,² and Anna Marie Pyle^{1,3,4,5,*}

¹Department of Molecular, Cellular, and Developmental Biology, Yale University, New Haven, CT 06511, USA

²Department of Molecular Biophysics and Biochemistry, Yale University, New Haven, CT 06510, USA

³Department of Chemistry, Yale University, New Haven, CT 06511, USA

⁴Howard Hughes Medical Institute, Chevy Chase, MD 20815, USA

⁵Lead contact

*Correspondence: anna.pyle@yale.edu

<https://doi.org/10.1016/j.celrep.2025.116739>

SUMMARY

Recent studies have uncovered a number of functional RNA structures in RNA viruses, yet their regulatory roles remain poorly understood. Here, using an unbiased proteomic approach alongside targeted biochemical assays, we investigate a previously uncharacterized functional pseudoknot (pk1) within the hepatitis C virus coding region and show that it stably interacts with host ribosomes, inhibiting translation and potentially acting as a regulator between viral translation and RNA genome replication. Comparative structural analysis identifies pk1-like elements in related RNA viruses, suggesting a conserved regulatory mechanism. This study expands the known functions of pseudoknots in viral coding regions beyond frameshifting, highlights the critical role of RNA structure-mediated regulation within viral open reading frames, and provides insight into the design of viral therapeutics and vaccines.

INTRODUCTION

Understanding the complex relationship between RNA structure and function has been a long-standing challenge in RNA virus biology. Over the past two decades, numerous functional RNA structures have been identified through genetic approaches, primarily within viral untranslated regions (UTRs) and their proximal regions. These include internal ribosome entry sites (IRES),^{1–4} nuclease-resistant pseudoknots,^{5,6} tRNA-like structures,^{7,8} viral packaging signals,⁹ and *cis*-replicating elements.^{10–13} These discoveries have significantly expanded our understanding of RNA structure-based regulation in viruses and beyond.

However, our knowledge of RNA structure-function relationships within viral open reading frames (ORFs) remains limited. While computational studies suggest that RNA viruses exhibit globally compact structures containing stable regulatory elements,^{14,15} experimental evidence and mechanistic insights are scarce. To date, the frameshifting pseudoknot remains the only well-characterized regulatory RNA structure within viral coding regions.^{16,17} This underscores the need for a systematic approach to identify and investigate novel RNA structures within ORFs of viral genomes and within mRNAs from bacterial and eukaryotic organisms.

Recent advances in high-throughput structure probing methods, such as Selective 2'-hydroxyl acylation analyzed by primer extension and mutational profiling (SHAPE-MaP) and dimethyl sulfate mutational profiling (DMS-MaP),^{18–21} have

significantly enhanced our ability to study long transcripts, such as viral genomes, thereby revealing a diversity of functional structures in viral coding regions, including those from severe acute respiratory syndrome coronavirus 2 (SARS-CoV-2), Dengue virus, West Nile virus, and hepatitis C virus (HCV).^{22–25} Despite these intriguing discoveries, the molecular mechanisms of these structures remain poorly understood, representing a largely unexplored area of research.

This knowledge gap is particularly important given the intense recent focus on mRNA and attenuated virus vaccines, such as nOPV2 (the engineered oral poliovirus vaccine), which has greatly improved the stability of the traditional OPV through rational engineering of the regulatory RNA structures in poliovirus.^{26,27} This advancement highlights the need for a deeper understanding of how RNA structures regulate translation efficiency, RNA stability, host evasion, and viral pathogenesis. Exploring the mechanisms of RNA structural motifs can guide the design of safer, more effective vaccines and mRNA therapies. Furthermore, since RNA viruses share many similarities with mRNA, discovering novel regulatory RNA structures in viral genomes can portend the existence of similar structures in human mRNAs and aid the development of broadly applicable structure-based regulation tools.

Recently, we probed the full-length RNA structure of HCV within infected human cells and identified numerous functional secondary and tertiary structures, including pseudoknots, in the viral coding region.²⁴ Among these many interesting motifs,



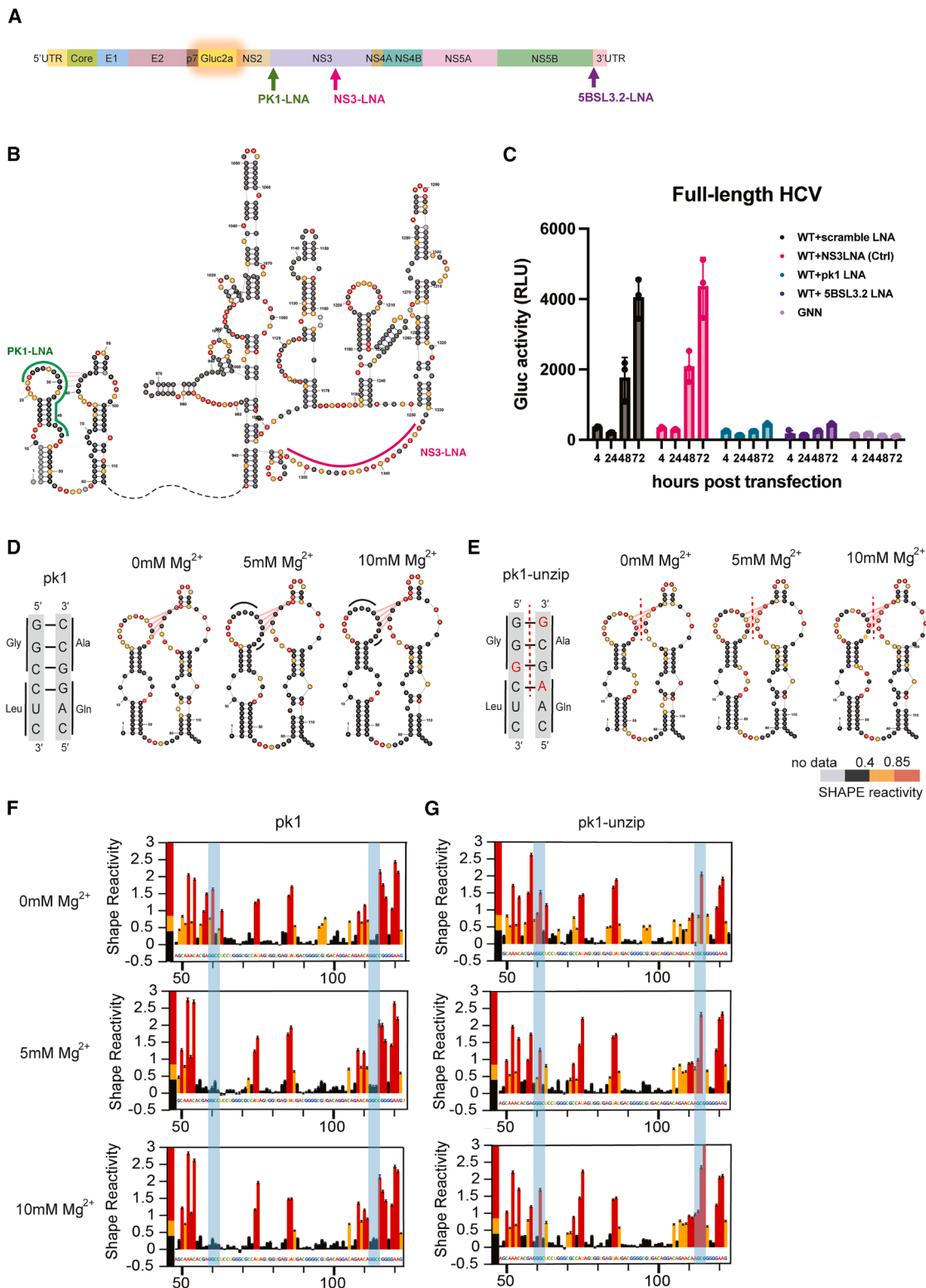


Figure 1. Pseudoknot1 (pk1) forms a compact structure and is critical for full-length HCV replication

(A) Schematic of the full-length HCV luciferase construct. Arrows indicate the genomic positions of structure-disrupting locked nucleic acids (LNA).

(B) Secondary structure map of HCV NS3 region labeled *in vivo* SHAPE reactivity (data from Wan et al.,²⁴ JV). The pk1 LNA is indicated by a green line, and the control LNA, targeting a downstream single-stranded region, is shown by a pink line.

(legend continued on next page)

we discovered a particular pseudoknot (pk1) that shows a very strong phenotype in regulating HCV viral growth.²⁴ Specifically, we found that disrupting pk1 with synonymous mutations significantly reduced HCV sub-genomic replicon (an HCV replicon system that excludes structural proteins) growth, while restoring the pseudoknotted base pairs with synonymous suppressor mutations fully rescued the phenotype, indicating that pk1 mediates a strictly structure-based regulatory mechanism, therefore meriting further exploration.²⁴

Here, we employed an unbiased proteomic approach alongside targeted biochemical assays to investigate the mechanism of action for pk1. We show that pk1 forms a compact structure both *in vitro* and *in vivo*. Disrupting this structure with locked nucleic acid (LNA) and synonymous mutations significantly reduces viral growth. Mass spectrometry-based pull-down assay revealed a direct interaction between pk1 and single ribosomes, suggesting a potential role in translation regulation. Consistent with this, luciferase reporter assays and polysome fractionation studies showed that pk1 inhibits both upstream and downstream protein expression by recruiting ribosome quality control factors, thereby rebalancing the RNA from the active translation phase to the RNA synthesis phase. An initial search for “pk1-like” elements identified similar structures in other RNA viruses, suggesting a potentially unexplored, widespread regulatory mechanism across RNA viruses and potentially other mRNA molecules.

Overall, our findings represent the only mechanistic study of RNA structures in coding regions since the discovery of frameshifting pseudoknots, highlighting the diverse roles pseudoknots can play beyond frameshifting. These structural insights will expand our understanding of the roles played by RNA structures in viral ORFs and are pivotal in designing novel viral therapeutics and vaccines. Additionally, the robust pipeline established in this study can serve as a roadmap for future research, applicable to other viral or human RNAs, elucidating diverse RNA structure functions and mechanisms under physiological or infection conditions.

RESULTS

pk1 forms a compact structure that regulates HCV growth

To understand the functional role of pk1 in the full-length HCV virus, we employed a well-established HCV luciferase reporter assay.^{28,29} As shown in Figure 1A, a *Gaussia princeps* luciferase (Gluc) reporter is inserted between the viral p7 and NS2 proteins, providing a quantitative measure of HCV replication.

To disrupt the functional RNA structure, we used anti-sense locked nucleic acids (LNAs) targeted to specific genomic RNA regions of interest. LNAs are non-natural base analogs that

enhance the melting temperature (T_m) of paired duplexes, allowing them to outcompete existing structures and disrupt them without interfering with ribosomal translation of the transcript. This strategy has been successfully employed to study functional RNA structures in multiple viruses.^{22,23,25,30} Based on the *in cellulo* HCV secondary structure model obtained through SHAPE-MaP from our previous study,²⁴ we designed a pk1-LNA to target the pseudoknotted region to maximize tertiary structure disruption (Figure 1B). A negative control LNA targeting a downstream single-strand region located in the NS3-encoding region (NS3-LNA) was also included to account for any effects solely due to LNA binding to the viral genome (Figure 1B), as in previous studies.^{22,25} An LNA targeting a known functional structure at the 3' end (5BSL3.2)^{30–32} and a lethal NS5B mutant (GNN) that disrupts the polymerase active site were also used as positive controls. We find that pk1-LNA completely abolished HCV replication, comparable to the effects observed with the replication-defective mutant (GNN) and the 5BSL3.2 positive control (Figure 1C). In contrast, NS3-LNA had no impact on viral growth compared to the scrambled LNA control. These results suggest that the tertiary structure of pk1 plays a critical role in the replication of full-length HCV.

To biophysically characterize the secondary structure and pseudoknot pairings of pk1 and to investigate its folding requirements, we produced a purified transcript containing the pk1 element by T7 RNA transcription from a DNA template. We then conducted biochemical folding studies on this RNA by varying Mg^{2+} concentrations and probing the pk1 secondary structure using SHAPE-MaP.¹⁸ The biochemically derived SHAPE reactivity data were obtained by high-throughput sequencing and then used as experimental constraints for secondary structure prediction with SHAPEKnots.³³ The pk1 structure and SHAPE reactivities obtained under biochemical conditions (Figure 1D, 5 mM and 10 mM Mg^{2+}) closely resemble those from full-length *in cellulo* HCV SHAPE-MaP structure determination (Figure 1B), indicating that pk1 can correctly fold by itself under purified conditions without additional HCV RNA sequence or protein components, suggesting it is an independent, compact structural unit.

Analysis of SHAPE reactivity under varying Mg^{2+} concentrations revealed that the pk1 pseudoknot exhibits magnesium-dependent folding. Specifically, we observed relatively high SHAPE reactivity at 0 mM Mg^{2+} in the left arm of the pseudoknot and significantly lower SHAPE reactivity in both the left and right arms of the pseudoknot at 5 mM and 10 mM Mg^{2+} . These findings indicate that pk1 undergoes magnesium-dependent folding and starts compacting at low magnesium concentrations (5 mM) (Figures 1D and 1F).

Looking carefully at the pseudoknotted region, we noticed that the left arm of pk1 has six additional nucleotides with low SHAPE

(C) Replication time courses for wild-type (WT) HCV treated with control LNA or pk1-targeting LNA, measured by Gluc activity. Data are represented as mean \pm SD of three biological replicates.

(D and E) Left: sequence of the WT or mutated pseudoknotted stem. Right: structural representation of pk1 or the unzip mutant labeled with *in vitro* SHAPE reactivity, obtained after folding in different concentrations of Mg^{2+} . The nucleotide position of the pseudoknotted left arm is 28–31 (position 4,046–4,049 in Jc1); the nucleotide position of the pseudoknotted right arm is 76–79 (position 4,099–4,102 in Jc1).

(F and G) Bar plot of the *in vitro* SHAPE reactivities obtained from pk1 and the pk1 unzip mutant under different concentrations of Mg^{2+} . The blue-shaded region highlights the left and right arms of the pseudoknotted stem.

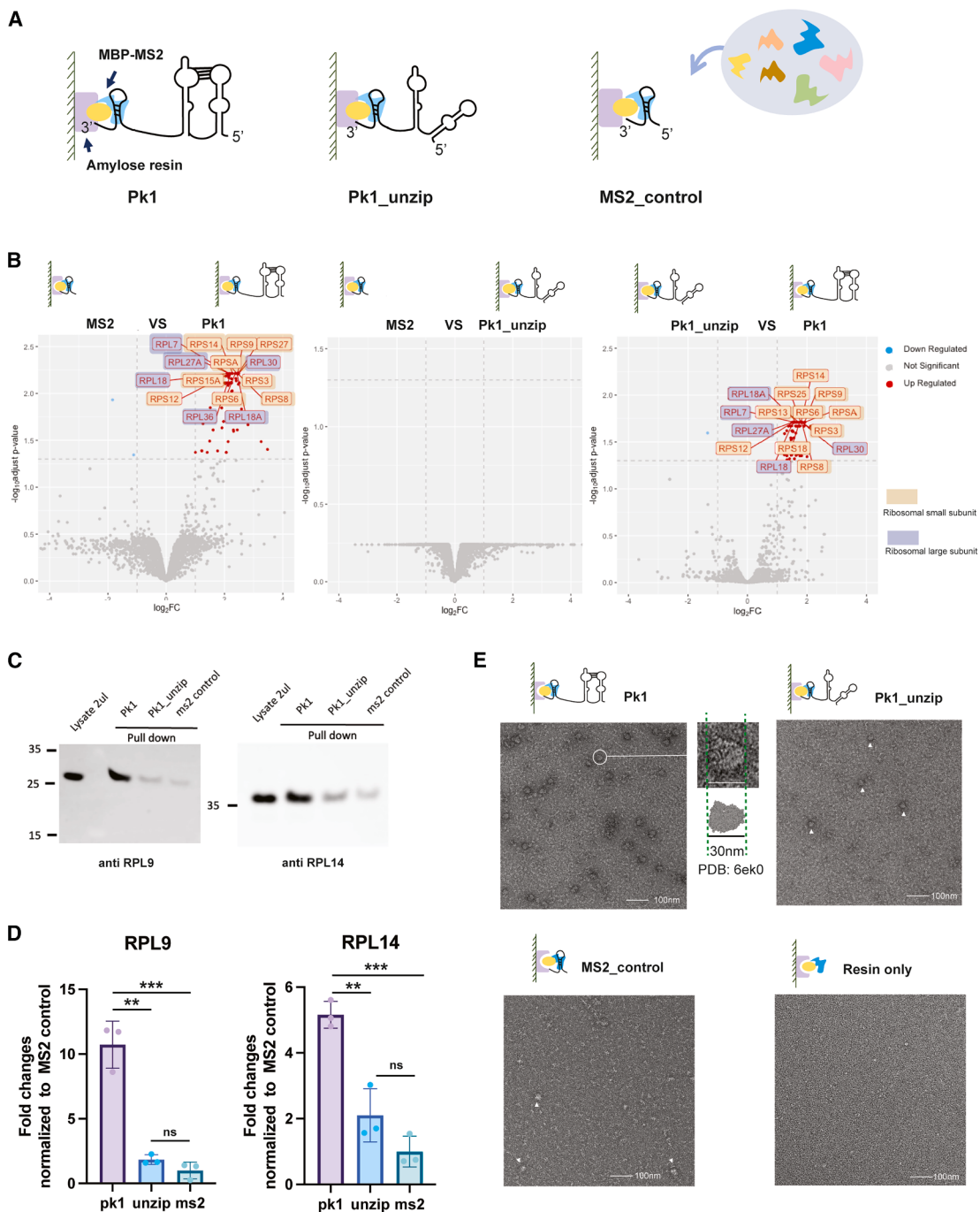


Figure 2. *In vitro* pull-down experiments suggest that pk1 interacts with the ribosome in a structure-specific manner

(A) Workflow of the *in vitro* MS2 pull-down approach used to discover proteins that bind pk1 RNA.
(B) Mass spectrometry quantification comparing pk1 pull-down versus MS2 control pull-down, pk1-unzip mutant versus MS2 control pull-down, and pk1 pull-down versus pk1-unzip pull-down. The top 15 significantly enriched proteins ($p_{\text{adjust}} < 0.05$) are labeled. Mass spectrometry pull-down experiments were performed in triplicate.

(C) Western blot analysis of RPL9 and RPL14 from pk1, pk1-unzip, and MS2 control pull-down elution samples. Experiments were performed in triplicate, with one representative replicate shown.

(D) Quantification of the western blots from (C). Data are represented as mean \pm SD of three biological replicates. Statistical significance was determined using an unpaired Student's *t* test with equal variance (** $p < 0.01$ and *** $p < 0.001$).

(legend continued on next page)

reactivities that fall outside of the pseudoknotted region (**Figure 1D**; 5 mM Mg and 10 mM Mg, black line). This observation is consistent with the *in cellulo* SHAPE-MaP results (**Figure 1B**) and suggests that the pseudoknot interaction might extend beyond the predicted four nucleotides, potentially involving non-canonical base-pairing interactions or compact tertiary base stacking that restricts the flexibility of the RNA backbone, leading to reduced SHAPE reactivity.

To further validate the pseudoknotted interaction site, we performed parallel *in vitro* folding studies on the pk1-unzip mutant. The pk1 unzipped mutant incorporates synonymous mutations to disrupt three of the four pseudoknotted base pairs and was previously shown to reduce HCV replicon replication to one-third that of the wild-type (WT).²⁴ We observed that both stems of pk1-unzip mutant exhibit low SHAPE reactivity, similar to WT-pk1, indicating that the overall secondary structure of pk1 remains intact in the pk1-unzip mutant. However, on both sides of the pseudoknotted arm, the pk1-unzip mutant displays high SHAPE reactivity across all tested magnesium concentrations, with only a slight reduction in reactivity within the left arm at 10 mM Mg²⁺, which may reflect subtle changes in the secondary structure of the left top loop (G28 and G29, **Figures 1E** and **1G**). These findings confirm the pseudoknotted interaction site and suggest that while the secondary structure is preserved, the tertiary structure of pk1 is well disrupted in the pk1-unzip mutant.

pk1 interacts with the ribosome in a structure-specific manner

To further elucidate the mechanistic function of the pk1 RNA element, we sought to investigate its RNA structure-specific interactome. As an unbiased approach, we employed an *in vitro* ribonucleoprotein pull-down assay to identify pk1 RNA-binding proteins (**Figure 2A**). In brief, three MS2 stem loops were appended to the 3' end of pk1; the RNA construct was folded in the presence of 10 mM Mg²⁺ and immobilized on amylose resin using an MBP-MS2 fusion protein. HCV-SGR (sub-genomic replicon) cell lysate, containing both host and HCV replicase proteins, was then applied to the resin to capture potential pk1-interacting proteins.

After capture, the MBP-MS2-RNA bait and associated proteins were eluted with maltose-containing buffer and analyzed via mass spectrometry to determine the identity of any RNA-binding proteins. Control experiments included parallel experiments using pk1-unzip mutants and MS2-only constructs (**Figure 2A**). In brief, a small aliquot of the elution sample was run on denaturing RNA and protein gels to verify the size of the bait RNA and MBP-MS2 protein (**Figure S1A**), respectively. Mass spectrometry was then performed with three biological replicates per pull-down, and quality control analysis indicated that 7 out of 9 samples provided sufficiently high-quality data for downstream analysis (**Figure S1B**). Significantly enriched proteins ($p_{\text{adjust}} < 0.05$, log₂ fold change [FC] > 1.5) were provided for each comparison (**Figure 2B**).

Notably, comparison of the pk1 pull-down with the MS2-only pull-down revealed a significant enrichment of ribosomal proteins from both the small and large subunits (**Figure 2B**, left). This suggests a potential interaction between pk1 and the ribosome. Given that ribosomes have an inherently high affinity for RNA, we sought to determine whether the interaction with pk1 is structurally specific by comparing the results with those from a pk1-unzip pull-down. We observed that ribosomal proteins were not enriched in the pk1-unzip control compared to the pk1 pull-down (**Figure 2B**, middle), indicating that the observed protein-RNA interactions are specific to the unique, 3D structural features of pk1. Importantly, no significant enrichment of proteins was observed in the pk1-unzip pull-down relative to the MS2 control pull-down (**Figure 2B**, right), indicating that the unzipped pseudoknot has no major affinity for RNA-binding proteins in this assay, and that all proteins binding to pk1 required the pseudoknotted structure of the element. The protein interactome with pk1 was further probed by western blot against two of the most highly enriched ribosomal proteins obtained from the mass spectrometry results, RPL9 and RPL14. The results indicate that both proteins are enriched significantly in the pk1 WT pull-down compared to pk1-unzip/ms2 pull-down (**Figure 2C**), with a 5- to 10-fold increase in the pk1 WT pull-down (**Figure 2D**).

To further explore the pk1 interactome, we examined significantly enriched non-ribosomal proteins from the pull-down experiments. Surprisingly, many of these non-ribosomal proteins have been implicated in ribosome biogenesis pathways, including factors essential for 60S and pre-40S maturation³⁴ (**Figure S1C**). Given that these proteins are predominantly nuclear and not typically associated with critical HCV life cycle events, we hypothesize that pk1 may also capture some immature ribosomes during pull-down due to structural similarities with mature ribosomes.

To visualize pk1-ribosome interactions and evaluate whether pk1 interacts with intact ribosomes, we conducted additional pull-down experiments using rabbit reticulocyte lysate and examined the elution samples by negative-stain electron microscopy. Ribosome particles of the correct size are clearly visible in samples from the pk1 pull-down (~35 per image), but few are observed in the pk1-unzip control (2–4 per image), MS2 control (2–4 per image), or resin-only samples (none observed) (**Figure 2E**). This collection of data confirms the interaction between pk1 and host ribosomes and suggests a potential regulatory role for pk1 in translation activity.

Pk1 significantly inhibits translation efficiency, with a critical role for the right stem

Since pk1 directly interacts with the host ribosome and is located at the beginning of an HCV genomic region that encodes replicase proteins, we initially hypothesized that pk1 might function as an IRES that initiates independent translation of this critical region of the HCV genome. To test this, we created a luciferase-based translation reporter construct and tested translation initiation from the pk1 element. Results from the reporter construct

(E) Negative stain images of pull-down eluates from pk1, pk1-unzip, MS2 control, and resin-only control samples. Ribosome-like particles are indicated with white arrowheads in the pk1-unzip and MS2 control samples. In the pk1 pull-down, ribosome-like particles are too abundant to label individually; instead, a zoomed-in image of one representative particle is shown and compared to the known 80S ribosome model (PDB: 6EK0).

indicate that pk1 does not initiate translation. Rather, pk1 significantly inhibits translation efficiency when compared with both the no-initiation controls (random control and empty control) and the HCV IRES control (Figure S2A), suggesting that, while pk1 can recruit ribosomes, it does not initiate protein synthesis events.

Given that pk1 is located within the HCV coding region, we next investigated a potential role in translation elongation. We inserted pk1 into the ORF of Gaussia luciferase and used the HCV IRES to initiate translation (Figure 3B, left). To ensure that the highly structured HCV IRES did not affect pk1 folding, we included a 99-nt linker sequence with low structural propensity between the HCV IRES and pk1. As controls, we used the pk1-unzip mutant and a randomized pk1, where the pk1 sequence was shuffled by three nucleotides, thereby maintaining the same amino acid composition as the WT pk1.

The RNA constructs described above were transfected into cells, and luciferase activity was measured at various time points to assess translation activity (Figure 3B, right). We observed that pk1 significantly inhibited translation elongation at all time points tested compared to the pk1-unzip and random controls. Notably, at 4 h post-transfection, there was nearly a 4-fold difference between the activity of pk1 and the pk1-unzip mutant, indicating that the pseudoknot structure itself, rather than just its constituent stems, is crucial for the observed translation inhibition (Figure 3B). To further examine the structural basis of this effect, we introduced a pk1-compensatory mutant that restores the disrupted base pairing in the pk1-unzip mutant using synonymous G-U wobble and A-U base pairs (sequence shown in Figure 3A). We performed an independent biological replicate and observed that the pk1 compensatory mutant mimics the pk1 phenotype relative to the unzip mutant, consistent with our initial results (Figure S2B). These data reinforce the interpretation that observed translation repression depends on the structural integrity of pseudoknot folding.

To evaluate the possibility that the relative inhibitory effect was solely due to the stability of the individual stem secondary structures, we performed minimal free energy predictions for the three constructs.³³ The resulting ΔG values are comparable, reinforcing the idea that inhibition is conferred by the specific tertiary structure of pk1 and its interaction with the host ribosome (Figures S2C–S2H).

The small 2-fold difference between the pk1-unzip mutant and the random control (Figure 3B) may be attributable to an incomplete disruption of the pseudoknot pairings within the pk1-unzip construct. This is consistent with the chemical probing data obtained during the *in vitro* folding studies described above, which suggested that additional loop nucleotides might contribute to tertiary interactions within the pseudoknot. Thus, the pk1-unzip mutant may partially fold *in vivo*, allowing it to retain a small inhibitory effect.

To address this, we designed a series of unzip constructs containing synonymous mutations that further disrupt the structure of pk1 (Figure 3A). Furthermore, to evaluate whether the observed translation inhibition is specific to IRES-mediated translation, we created a second parallel system, in which a type I cap is used to initiate translation (Figure 3C). The resulting

luciferase activity indicates that as we progressively unzip the pk1 structure, its translation-inhibitory activity gradually decreases, approaching the translation activity of the random control (Figure 3C). Consistent with the IRES-initiated translation results, we observed a 2- to 4-fold difference between pk1 and the unzip mutants in the cap-dependent system, suggesting that pk1 mediates translation inhibition for both cap and IRES-mediated translation. Importantly, among all the mutants, we observed that unzipping the right stem (unzipR) exhibited the largest effects on alleviating translation inhibition, indicating that the right stem of pk1 plays an important role in translation inhibition activity (Figure 3C).

Next, we wanted to examine how the various pk1 unzip structural mutations affect full-length HCV growth. To do this, we introduced the same pk1 synonymous mutants (Figure 3A) into the full-length HCV luciferase construct (Figure 3D). Luciferase activity was measured at 24, 48, and 72 h post-transfection to assess initial HCV growth in the cells. We observed that the pk1 unzip mutants exhibit the growth defect as early as the 24-h time point. This defect persists and becomes more pronounced through 72 h post-transfection, at which point we observed a 2- to 3-fold decrease in luciferase signal for the unzip mutants relative to WT HCV (Figure 3E), confirming that the pk1 RNA 3D structure plays an important role for viral growth. Interestingly, unzipping the pk1 structure produced a similar trend in full-length viral growth (Figure 3E) as observed in the *in vitro* translation assays (Figure 3C). Notably, among all the mutants, unzipping the right stem of pk1 (unzipR) had the most pronounced effect, consistent with the translation assay results (Figure 3C), further highlighting the critical role of the pk1 right stem in translation inhibition and overall viral growth. To further confirm that pk1 mutants affect RNA levels of full-length HCV, we performed quantitative reverse-transcription PCR (RT-qPCR) at 72 h post-transfection. We observed that the unzip, unzipL, and unzipR mutants exhibited significantly reduced viral RNA levels compared to WT HCV, indicating that RNA replication is impaired in these pk1 mutants (Figure S2J).

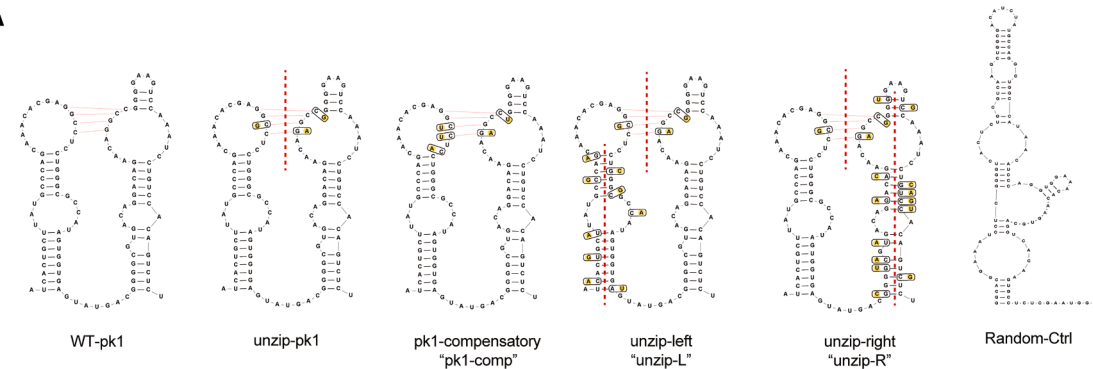
Pk1 inhibits translation activity independent of its location on the transcript

The observations above suggest that pk1 can significantly inhibit translation activity. Given that pk1 is positioned at the junction between the set of HCV structural proteins and the essential replicase proteins, we wondered if its influence was position-specific and whether pk1 might specifically inhibit downstream protein expression and thereby regulate the ratio of structural to replicase proteins.

To test this hypothesis, we designed a dual-luciferase construct where pk1 was inserted between two luciferase genes. An FMDV 2A ribosome-skipping sequence was placed after the first luciferase to reinitiate translation of the second luciferase (Figure 4A). To our surprise, results from the dual-luciferase assay at 2 h post-RNA transfection show that pk1 inhibits both upstream and downstream translation to a similar extent for both IRES (~60% of control) and cap (~40% of control) initiated translation (Figures 4A and S3A).

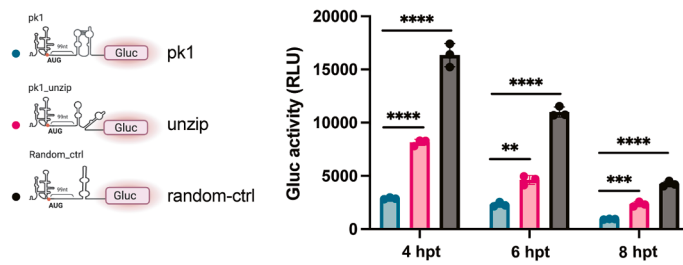
To test whether the inhibition of upstream protein expression is related to the relative distance between pk1 and the upstream

A

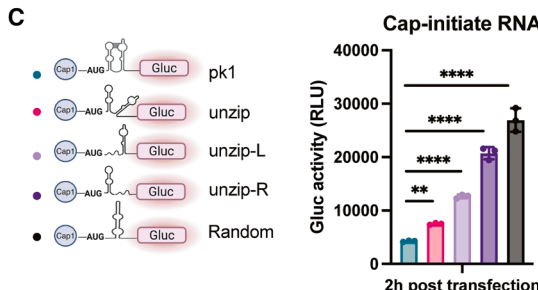


B

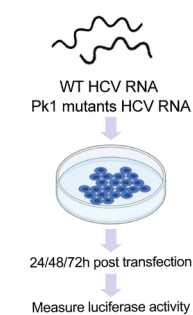
IRES-initiate RNA



C



D



E

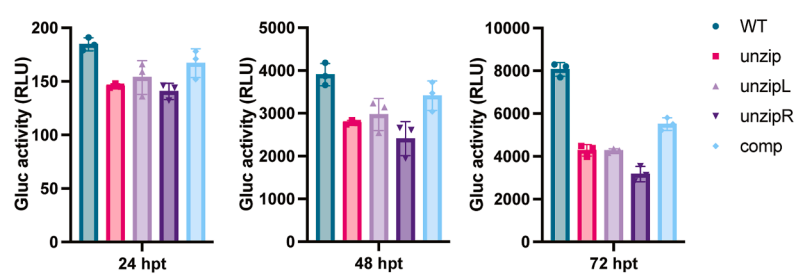


Figure 3. pk1 plays a critical role in translation inhibition and viral growth

(A) Schematic of the WT pseudoknot and structure-disrupting mutants.

(B) Luciferase activity of IRES-driven constructs measured over time; construct designs shown on the left.

(C) Normalized luciferase activity of various IRES-driven constructs at different time points, relative to the random control; construct designs shown on the left.

(D) Workflow for full-length HCV growth assay.

(E) Measurement of WT and mutant viral growth by luciferase activity at 24, 48, and 72 h post-transfection.

Data are represented as mean \pm SD of three biological replicates. Statistical significance was determined using an unpaired Student's *t* test with equal variance (***p* < 0.01, ****p* < 0.001, and *****p* < 0.0001).

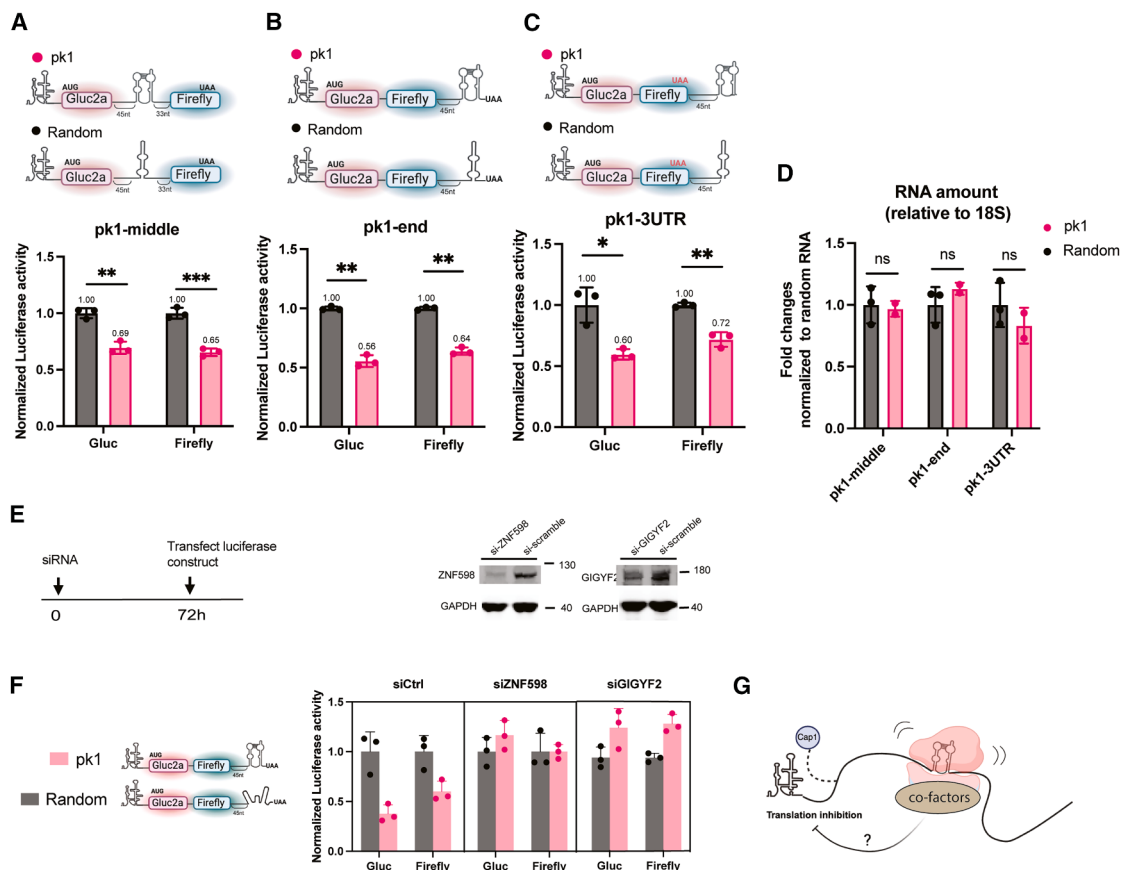


Figure 4. Pk1 inhibits translation activity independent of its location by activating protein cofactors

(A–C) Top: Schematic of the dual luciferase constructs used to test pk1's regulation of upstream and downstream protein expression. Bottom: Gaussia and Firefly luciferase activities for pk1 and random control constructs, measured at 2 h post-transfection and normalized to the random control.

(D) qPCR quantification of Actin mRNA or luciferase construct RNA amount relative to 18S rRNA for each sample, normalized to the random control RNA.

(E) Left: siRNA knockdown workflow. Right: western blot analysis of ZNF598, GIGYF2, and GAPDH confirming siRNA knockdown efficiency.

(F) Gaussia and Firefly luciferase activities after siRNA treatments for pk1 and random control constructs, measured at 2 h post-transfection and normalized to the random control. The inhibitory effect in the siCtrl condition for the pk1-middle construct was weaker than in previous experiments (Figure 3), possibly reflecting variability in RNA input associated with the siRNA transfection setup and limited time point sampling.

(G) Graphic showing the proposed pk1 inhibiting translation initiation mechanism.

Data are represented as mean \pm SD of three biological replicates. Statistical significance was determined using an unpaired Student's *t* test with equal variance (* $p < 0.05$, ** $p < 0.01$, *** $p < 0.001$, and **** $p < 0.0001$).

protein and can therefore result from potential ribosome stalling, we moved pk1 to the end of the ORF, downstream of both luciferase proteins. However, we still observed a large inhibitory effect for the expression of both luciferase proteins (~60% of control) (Figures 4B and S3B).

To further evaluate whether the inhibitory effect is independent of ribosome stalling and the relative location of pk1, we placed pk1 in the 3' UTR of a dual-luciferase construct, 45 nucleotides from the stop codon. Even in this position, pk1 still exerted a large inhibitory effect on both types of luciferase (~60%–70% of control) (Figure 4C) in both IRES-mediated and cap-initiated translation (~50% of control, Figure S3C). Notably, RT-qPCR analysis of luciferase RNA showed comparable RNA levels between pk1 and random control constructs (Figures 4D and S3D), suggesting that the RNA template remains intact despite the translation inhibition. We also harvested a sample at 4 h

post-transfection for all experiments described above, and we noticed a similar trend of translation inhibition of both upstream and downstream proteins. This result indicates that the transfected RNA remains stable and that observed translation inhibition persists after 4 h in cells (Figures S3E–S3J).

Collectively, these results indicate that pk1 consistently reduces protein expression through the action of a single RNA motif irrespective of its location along the transcript, suggesting a uniquely powerful mechanism of translation inhibition. To explore this further, we investigated well-characterized factors that are involved in the ribosome quality control pathways that inhibit translation initiation while still preserving RNA integrity. Based on this analysis, we chose to target ZNF598, an early marker of aberrant ribosomes,^{35,36} and GIGYF2, a factor recruited by ZNF598 to inhibit translation initiation while preserving RNA integrity,^{35,37} using siRNA knockdowns (Figure 4E).

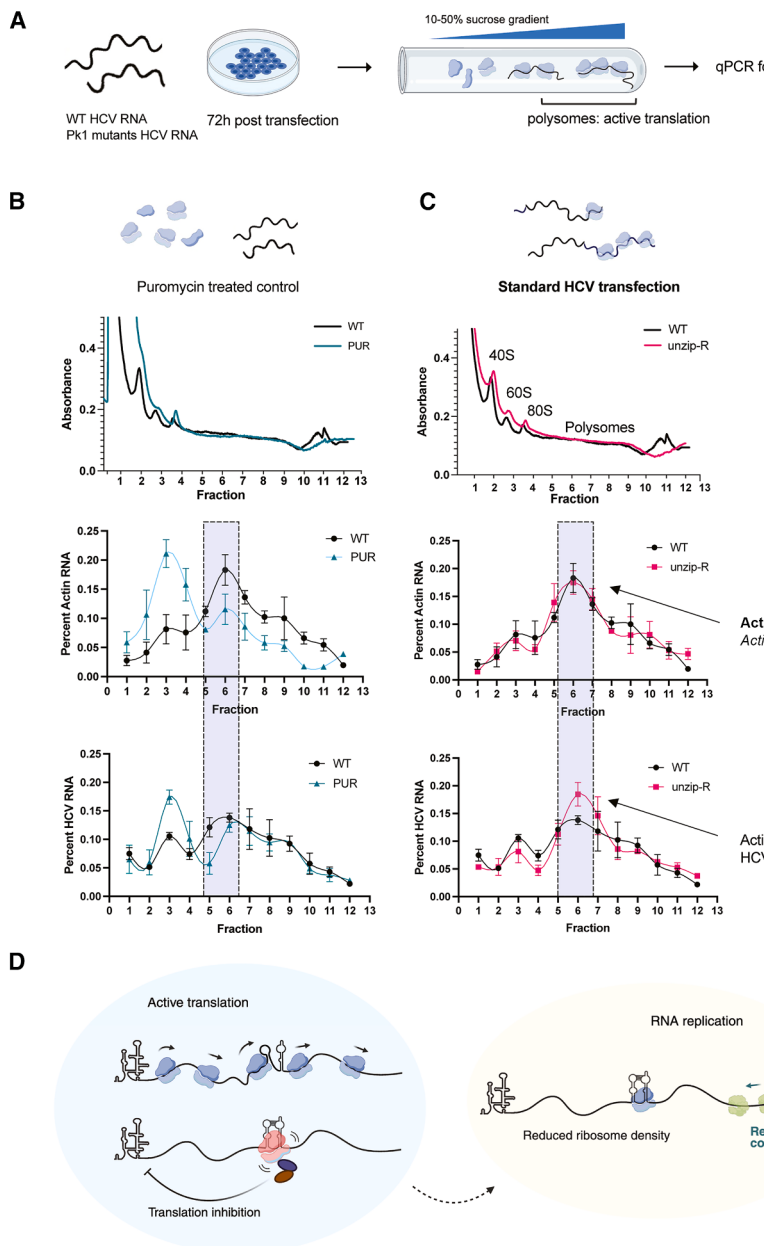


Figure 5. Pk1 rebalances HCV RNA from active translation to RNA synthesis

(A) Workflow of polysome fractionation and RNA quantification for HCV-transfected cells.

(B) Top: chromatogram showing the separation of monosome and polysome fractions. Middle: distribution of *Actin* mRNA across all fractions in WT and PUR-treated control. Bottom: distribution of HCV RNA across all fractions in WT virus and PUR-treated control.

(C) Top: chromatogram showing the separation of monosome and polysome fractions. Middle: distribution of *Actin* mRNA across all fractions in WT and unzip mutant virus. Bottom: distribution of HCV RNA across all fractions in WT virus and unzip mutant virus.

(D) Graphic showing the proposed pk1 acting mechanism.

region. Overall, our data suggest that pk1 contributes to translation in collaboration with protein cofactors such as ZNF598 (Figure 4G). Future investigation could explore additional factors involved, especially when pk1 is located at different positions on the RNA, to further elucidate the underlying inhibitory mechanism.

Pk1 facilitates the shift of HCV RNA from active translation to RNA synthesis

To understand how the translation-inhibitory effect of pk1 contributes to overall viral growth, we assessed its impact on viral RNA distribution between the active translation and replication phases using polysome fractionation analysis. Huh7.5 cells were transfected with full-length HCV RNA or the pk1-unzipR mutant, and 72 h post-transfection, the cells were harvested for polysome fractionation (Figure 5A). Monosome and polysome fractions for each of the constructs were successfully separated and analyzed (Figures 5B and 5C, top). We also included the polysome profile of untreated Huh7.5 cells as a control. Compared to untreated cells, both HCV infection and puromycin treatment reduced polysome abundance (Figure S5), consistent with the previous reports.^{38–40} For a benchmark, we included a control treated with puromycin, which induces the dissociation of polysomes from mRNA, thereby creating a “non-translating RNA” condition. As expected, puromycin treatment caused both actin mRNA and HCV RNA to shift from the polysome to the monosome fraction, confirming the ability of the assay to distinguish between actively translating and non-translating RNA (Figure 5B).

Comparison of the WT HCV with the pk1-unzipR mutant shows that the unzipped mutant displays a higher proportion of RNA in the actively translating polysome fraction and less in

After 72 h of siRNA treatment, we transfected the dual luciferase RNA construct. At 2 h post-transfection, we performed the dual luciferase assay and observed that knocking down ZNF598 partially rescues the inhibition phenotype for pk1-middle construct, pk1-end constructs, and pk1-UTR constructs, suggesting its involvement in pk1-mediated translation inhibition (Figures 4F, S4A, and S4B). In contrast, knocking down GIGYF2 rescues the inhibition phenotype for the pk1-middle construct and pk1-end construct but only by less than 10% for the pk1-UTR construct (Figures 4F, S4A, and S4B). This suggests that GIGYF2 contributes to pk1-mediated translation inhibition primarily when pk1 is located within the ORF, while other cofactors may cooperate with ZNF598 when pk1 resides in the UTR

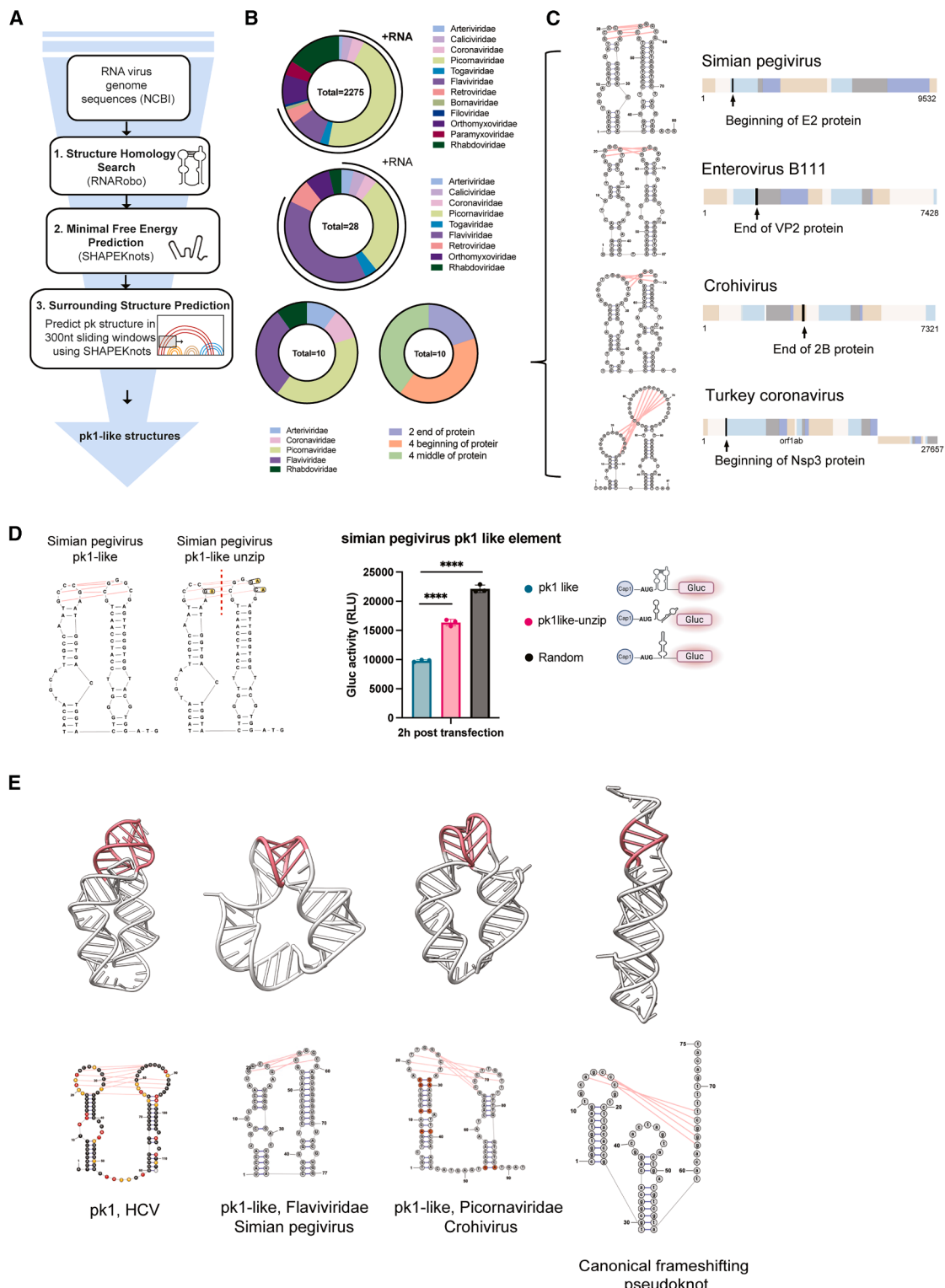


Figure 6. Pk1-like structures exist broadly in diverse virus families, and they exhibit a specific type of tertiary conformation

(A) Workflow for identifying pk1-like elements across RNA virus genomes.

(B) Top: pie chart summarizing the family distribution of input viruses. Middle: pie chart showing the family distribution of viruses identified after step 2. Bottom: pie chart displaying the family distribution and location of pk1-like elements after step 3.

(C) Examples of high-confidence pk1-like elements located near viral protein boundaries.

(legend continued on next page)

the monosome fraction. This suggests that pk1 may shift RNA from active translation toward RNA synthesis (Figure 5C, bottom). Notably, actin RNA remains in the polysome fractions, indicating that the apparent transcript regulation is specific to the HCV viral RNA in these cells (Figure 5C, middle). Taken together with the results from the previous section, these findings suggest that pk1 may stall or bind ribosomes. We hypothesize that the observed translation suppression may serve a positive role at specific stages of the viral life cycle, as it would enhance the ability of the replication complex to bind the template, successfully initiate strand synthesis, and carry out replication (Figure 5D).

Pk1-like structures are broadly present across viral families and adopt a specific type of tertiary conformation

To investigate whether a “pk1-mediated translation inhibition” mechanism is common across different viral families, we developed a preliminary pipeline to identify pk1-like structures in RNA viruses (Figure 6A). This approach begins with a structure homology search in which RNARobo⁴¹ is used to identify structural elements that appear similar to HCV-pk1 (Figure S6). Based on the information gleaned from our structural and biochemical characterization of the HCV RNA, we prioritized a stringent search based on pseudoknotted stems (e.g., stem h3, Figure S6) and we restricted base-pairing interactions to contain stable G-C pairings. The resulting hits were then subjected to minimal free energy predictions using SHAPEKnots⁴² to ensure that the pk1-like structures were energetically favorable. Finally, to confirm that the pk1-like structures could be predicted in the context of their surrounding sequences, we performed surrounding structure predictions with SHAPEKnots, using five ~300-nt windows to cover the pk1-like regions. A pk1-like structure was considered valid if it was observed in at least one window and was calculated to have a highly favorable folding free energy. These steps helped to ensure a rigorous and stringent search for pk1-like structures.

As an initial test, we analyzed a small database of 2,275 full-length RNA viral genome sequences from the NCBI RefSeq database. After structure homology searches and minimal free energy predictions, we identified 28 potential pk1-like structures, primarily within the *Flaviviridae* and *Picornaviridae* families. Further structural predictions of the surrounding regions yielded 10 high-confidence pk1-like structures, all located within the viral coding regions. Notably, six of these were positioned at the start or end of sequences encoding viral proteins (Figures 6B and 6C; full list shown in Table S2; Figure S7).

Three representative hits from the *Flaviviridae* family were observed in a *Pegivirus*: at the beginning of the Simian Pegivirus E2 protein (Figure 6C, top), at the start of the GB virus envelope protein (Figure S7), and within the middle of the Norway rat pegivirus polyprotein (Figure S7), respectively. Pegiviruses share a similar genomic organization with HCV and are known to cause

persistent infections in humans, much like HCV.⁴³ This resemblance suggests that further investigation could be performed into the prevalence of pk1-like elements in pegiviruses and that one should consider their potential role in persistent human infections. Additional high-confidence elements were found in *Picornaviridae*, located at the end of Enterovirus VP2 or at the end of Crohivirus 2B proteins, and in *Coronaviridae*, at the start of Nsp3 protein (Figure 6C).

To determine whether the pk1-like elements identified in other viruses mediate translation inhibition, we selected the top hit, which is the pk1-like element from Simian Pegivirus, and assessed its translation activity using a luciferase reporter assay. As a control, we introduced synonymous unzipping mutations to disrupt the pseudoknotted tertiary interaction (Figure 6D). The results show that the pk1-like element in Simian Pegivirus significantly inhibits translation activity compared to the unzipped mutant and random control. Specifically, there is a >1.5-fold difference in translation activity between the pk1 and pk1-unzip mutant, and a >2-fold translation activity difference between the pk1 and random control, suggesting that the pk1-like structure in Simian Pegivirus can behave similarly to HCV pk1 in modulating translation inhibition.

This analysis indicates that pk1-like pseudoknots likely represent a specific class of pseudoknot structures with defined conformations and translation-inhibiting functions. To investigate pk1 conformational features, we used AlphaFold3 to predict the tertiary structures of pk1 and pk1-like elements and compared them with the well-studied canonical coronavirus frameshifting pseudoknot. AlphaFold3 correctly predicted the pseudoknot base pairing interactions in pk1, including additional non-canonical base interactions between the two loops (Figure 6E, left, highlighted in pink in the 3D model and red in the secondary structure model). Notably, pk1 adopts a ring-like, two-helix conformation, in which the stem helices are connected by pseudoknot pairings and linker nucleotides. A similar conformation was predicted for pk1-like elements in flaviviruses and picornaviruses (Figure 6E, middle). In contrast, the canonical frameshifting pseudoknot from coronavirus has a different type of tertiary structure, characterized by a coaxially stacked single-helix conformation (Figure 6E, right). This difference suggests that pk1-like elements and frameshifting elements adopt distinct tertiary structures tailored for their different translation regulatory functions. Taken together, our results show that pk1-like elements are broadly present across RNA viruses, adopt specific conformations, and play specialized roles in translation inhibition, representing a defined class of pseudoknot motifs that merit further exploration.

DISCUSSION

As new experimental and computational tools are being implemented to analyze the wealth of data on RNA transcriptomes,

(D) Left: secondary structure representation of a pk1-like motif in Simian pegivirus and the design of the unzipped mutant. Right: translation luciferase activity illustrating the function of pk1-like element in translation elongation, measured at 2 h post-transfection. Construct design is shown on the right. Data are represented as mean ± SD of three biological replicates. Statistical significance was determined using an unpaired Student's *t* test with equal variance (**p* < 0.01, ***p* < 0.001, and ****p* < 0.0001).

(E) AlphaFold3 prediction of tertiary structures for pk1, pk1-like elements, and a canonical frameshifting pseudoknot. The corresponding secondary structures derived from the tertiary models are shown below.

it is becoming increasingly clear that stable RNA structural elements are pervasive in mRNA molecules, particularly those encoded by RNA viruses. Genetic and phylogenetic analysis suggests that many of these elements are functional, but in a few cases, a specific molecular mechanism is determined, particularly for structures located within the vast ORFs that encode protein sequences. Here, we report the first mechanistic characterization of an ORF RNA structural motif since elucidation of frameshifting pseudoknots. Building on a discovery pipeline for identifying functional RNA structures within the ORF of the HCV genome, we selected a particularly conserved RNA motif (pk1) and subjected it to detailed mechanistic analysis to identify its binding partners and influence on gene expression. Through this process, we have identified a specialized type of RNA pseudoknot that specifically reduces the efficiency of translation without altering the reading frame or the stability of the mRNA template. Identification and characterization of the PK1 control element underscores the likely diversity of riboregulatory motifs within the ORFs of protein-coding genes, and suggests a pipeline for their discovery and application.

A single reading frame contains more than one type of information

One of the most important implications of our findings is that two different types of information can coexist within the same section of the genetic code: protein sequence, embedded in the codons of RNA primary sequence; and regulatory information, embedded in the 2D or 3D structure of the RNA. This is significant because RNAs are typically considered to be strictly either informational (coding) or structural (noncoding). However, our study contributes to the growing evidence that this is a false dichotomy and that the same RNA sequence can contain more than one type of information or function. Such a broader view of RNA molecules, and of mRNAs in particular, opens up a wealth of opportunities for riboregulation, with important implications for synthetic biology and for therapeutics. It has long been known that the third nucleotide of a codon is almost completely variable, and the second is relatively permissive. Thus, ORFs have evolved to balance multiple types of fitness constraints at both the sequence and structural levels. Not unexpectedly, the small genomes of RNA viruses necessitate the full exploitation of this potential for multidimensional diversification.

The role of pk1 in regulating viral translation and replication

The search for molecular regulators that influence the transition of viral RNA through different stages of the viral life cycle has long been a focus in the field of positive-strand RNA viruses. While multiple regulating elements have been identified at viral termini, such as miR-122 in HCV,⁴⁴ 5BSL3.2 in the HCV 3' end,³⁰ cloverleaf elements in poliovirus,⁴⁵ and 5' terminal structure in bromo mosaic virus,^{46,47} no elements have been found in the viral coding region. Here, we propose that during viral translation, the pk1 structure, located in the middle of the HCV coding region, may bind a stalled ribosome and trigger translation inhibition. We hypothesize that the resulting reduction in ribosome density on the RNA may facilitate the transition to negative-strand synthesis, potentially supporting viral replication. These findings expand the

scope of translation-replication modulators to the viral ORF and suggest translation regulators may exist elsewhere in viral genomes. The presence of pk1-like elements in a range of RNA viruses, particularly in viruses associated with persistent infections, also indicates that this could be a broad regulatory mechanism that may help chronic viruses to reduce host translation stress and evade the host immune system.

Location specificity of pk1 and pk1-like elements in viral ORFs

The position of pk1 is notable, as it is located precisely between the genes that encode proteins essential for HCV replication and those that encode the viral structural proteins. We find that the majority of high-confidence pk1-like elements are also situated at or near boundaries between viral proteins. These include locations between two structural proteins (e.g., Enterovirus B111 and Simian Pegivirus) or between two non-structural proteins (e.g., Crohivivirus and Turkey coronavirus), but there appears to be no consistent pattern in the identity of upstream and downstream proteins. Due to the limited number of input viral sequences in our analysis, we were only able to confidently predict 10 pk1-like elements for location analysis. Future research could increase the number of viral genomes analyzed to further investigate whether the pk1-like motif tends to localize within the ORFs.

Nonetheless, we show that pk1 inhibits translation independently of its location on the template. This observation cannot explain why pk1 and pk1-like elements consistently occupy such unique positions within viral RNAs, and suggests that these elements may have additional, location-dependent roles beyond modulating translation and replication. For instance, pk1 elements might serve to slow the translation of the HCV polyprotein at critical positions, facilitating co-translational folding or cleavage of downstream proteins. These hypotheses underscore the multifaceted interplay of pk1 elements and their surrounding proteins, suggesting the potential utility of targeted antiviral therapies aimed at disrupting pk1 elements.

Implications for translation stalling studies

Translation stress is a critical challenge for cells, particularly during viral infections, as non-optimal codons and complex RNA structures can slow translation and activate ribosome quality control (RQC) pathways.³⁶ Here, we show that a regulatory structure in HCV (pk1) attenuates translation of its own RNA. We hypothesize that this inhibition may benefit HCV replication, as the pk1-unzip mutant exhibits a growth defect and shows increased association with actively translating ribosomes. This provides another example of how viruses repurpose host translation systems, as observed in SARS-CoV-2 and HIV,⁴⁸ and offers new insights into fine-tuning viral protein synthesis.

We observed that cap-dependent RNAs show stronger translational inhibition than IRES-driven RNAs across all three construct types (pk1-middle, pk1-end, and pk1-3' UTR). We hypothesize that the absolute level of inhibition may depend on the strength of translation initiation. Our preliminary experiments show that knockdown of ribosome-associated quality control factors such as ZNF598 and GIGYF2 can modestly alleviate the pk1 inhibitory phenotype in some contexts (Figures 4F and S4). These findings raise the possibility that pk1-mediated

translation inhibition may intersect with known RQC pathways, even though the precise mechanistic links remain uncertain. While the ZNF598 and GIGYF2 knockdown data presented in this study support the involvement of ribosome-associated quality control in pk1-mediated translation inhibition, multiple mechanisms may act in parallel. For example, through ribosome sequestration, pk1 may cause local reduction of 43S, which is known to be specifically involved in HCV IRES-mediated translation.⁴⁹ Further studies will be required to test whether RQC factors, ribosome sequestration, or other mechanisms underlie the effects of pk1.

While the precise pathways require further investigation, our study highlights the importance of RNA structure-induced ribosome stalling, an area largely unexplored compared to sequence-based stalling (polyA sequence) or antibiotic-induced collisions (e.g., anisomycin).³⁵ In this way, pk1 may provide a useful model system for studying general mechanisms of RNA structure-induced ribosome stalling.

Implications for RNA-based therapeutics

In the development of RNA-targeted antiviral therapeutics, most efforts have focused on modulating RNA structures within the UTRs. For example, modifications of the critical RNA structures in UTRs, guided by empirical observations or phylogenetic analyses, have been used to weaken viral replication in traditional live-attenuated vaccines.²⁶ Our study on RNA structures in the ORF and their underlying mechanisms offers opportunities to redesign live-attenuated vaccines by selective design of the coding region. Compared with mutations in the UTR sequences, modifications in the ORF would significantly reduce the risk of reversion mutations, making live attenuated vaccines safer and more effective.

For mRNA vaccines that deliver mRNA encoding viral structural proteins to stimulate immune responses, current designs have focused on enhancing RNA stability for easier transportation and storage.⁵⁰ However, this strategy often overlooks the impact of RNA structure on translation efficiency. Our findings show that certain RNA structures can significantly reduce translation efficiency, potentially limiting vaccine efficacy. This highlights the need for mRNA vaccine design that balances RNA stability with the potential impact of structures on translation efficiency.

This study elucidated the mechanistic role of a translation regulatory element that was selected from a pipeline for characterizing the secondary structure of full-length viral genomes. Our approach is suitable for characterizing the mechanism of unknown RNA structural motifs and is applicable to a variety of RNA viruses and human RNAs. It is hoped that this approach may encourage further functional exploration of hidden or overlooked RNA structures within the coding regions of mRNA. The accumulation of additional structural and mechanistic data will facilitate the rational design of mRNA vaccines and therapies, the improvement of attenuated virus vaccines, and the creation of RNA molecular tools, paving the way for the next generation of RNA-based therapeutics and research.

Limitations of the study

Our study does not directly establish that pk1 functions as a regulatory switch between translation and replication, and we also

did not directly assess its role in HCV replication or translation in the context of full viral infection. Several potential models could be relevant under infection conditions and may merit further study. For example, pk1 may adopt different conformations during the viral life cycle, much like a riboswitch, or it may bind different viral or host proteins during specific stages of viral infection, thus affecting its ability to remain stably bound with host ribosomes and activating the translation inhibition pathway. To resolve many of these issues, it may be valuable to investigate how pk1 affects native HCV protein translation to explore its potential role in co-translational regulation. These hypotheses highlight the importance of examining the pk1 structure and its interactome in infectious cells during the course of future investigations.

While polysome profiling provided valuable insights into the distribution of viral RNA between translationally active and inactive states in this study, we acknowledge that this approach remains an indirect measure of translation. Polysome fractionation is a widely used proxy in the translation field, but it cannot fully resolve potential confounding effects such as differences in RNA abundance.

RESOURCE AVAILABILITY

Lead contact

Further information and requests for resources and reagents should be directed to and will be fulfilled by the lead contact, Anna Marie Pyle (anna.pyle@yale.edu).

Materials availability

No unique reagents were generated in this study.

Data and code availability

- All ShapeMapper outputs, mass-spec analysis output, and secondary structure files used in this work are provided in the [supplemental information](#).
- No custom code was generated for this work.
- Any additional information required to reanalyze the data reported in this paper is available from the [lead contact](#) upon request.

ACKNOWLEDGMENTS

We thank Dr. Brett Lindenbach for his insightful discussions on this work and for sharing HCV-related constructs, cell lines, and access to the BSL-2+ lab. We also thank Ananthanarayanan Kumar, Benjamin Götte, Rafael de Cesaris Araujo Tavares, Lucille Tsao, Li-tao Guo, and Nicholas C. Huston from the Pyle lab for their thoughtful comments and discussions. Some schematic elements in [Figures 3 and 5](#) were created with [BioRender.com](#). This work was supported by the Howard Hughes Medical Institute, the National Human Genome Research Institute (HG011868 to A.M.P.), the National Institutes of Health grant (R01GM132358 to W.V.G.), the National Science Foundation (NSF 2330451 to W.V.G.), the National Science Foundation GRFP (DGE2139841 to K.S.A.), and the HHMI Gilliam Fellowship (to K.S.A.). Funding for open access charges was provided by the Howard Hughes Medical Institute. A.M.P. is an investigator with the Howard Hughes Medical Institute.

AUTHOR CONTRIBUTIONS

H.W., H.J., L.X., and K.S.A. conducted the experiments; H.W., H.J., L.X., K.S.A., and A.M.P. designed the experiments; H.W., H.J., L.X., K.S.A., W.G., and A.M.P. interpreted the data; and H.W., H.J., K.S.A., and A.M.P. wrote the paper.

DECLARATION OF INTERESTS

The authors declare no competing interests.

STAR★METHODS

Detailed methods are provided in the online version of this paper and include the following:

- KEY RESOURCES TABLE
- EXPERIMENTAL MODEL AND STUDY PARTICIPANT DETAILS
- METHOD DETAILS
 - Construct design and preparation
 - Pk1 RNA *in vitro* transcription, folding, and SHAPE modification
 - Reverse transcription, library preparation and data analysis for *in vitro* SHAPE-MaP
 - Full-length HCV growth luciferase assay
 - *In vitro* RNP pull-down
 - Pull-down experiment
 - Mass spectrometry and data analysis
 - Western Blot
 - Visualizing pk1 binding with ribosome using negative stain
 - Translation luciferase assay
 - Translation dual luciferase assay
 - siRNA knockdown
 - Polysome profiling experiment
 - *In silico* structure prediction pipeline
- QUANTIFICATION AND STATISTICAL ANALYSIS

SUPPLEMENTAL INFORMATION

Supplemental information can be found online at <https://doi.org/10.1016/j.celrep.2025.116739>.

Received: April 9, 2025

Revised: July 31, 2025

Accepted: November 25, 2025

REFERENCES

1. Berry, K.E., Waghray, S., and Doudna, J.A. (2010). The HCV IRES pseudo-knot positions the initiation codon on the 40S ribosomal subunit. *RNA* 16, 1559–1569. <https://doi.org/10.1261/rna.2197210>.
2. Quade, N., Boehringer, D., Leibundgut, M., van den Heuvel, J., and Ban, N. (2015). Cryo-EM structure of Hepatitis C virus IRES bound to the human ribosome at 3.9-A resolution. *Nat. Commun.* 6, 7646. <https://doi.org/10.1038/ncomms8646>.
3. Fraser, C.S., and Doudna, J.A. (2007). Structural and mechanistic insights into hepatitis C viral translation initiation. *Nat. Rev. Microbiol.* 5, 29–38. <https://doi.org/10.1038/nrmicro1558>.
4. Jan, E., and Sarnow, P. (2002). Factorless ribosome assembly on the internal ribosome entry site of cricket paralysis virus. *J. Mol. Biol.* 324, 889–902. [https://doi.org/10.1016/s0022-2836\(02\)01099-9](https://doi.org/10.1016/s0022-2836(02)01099-9).
5. MacFadden, A., O'Donoghue, Z., Silva, P.A.G.C., Chapman, E.G., Olszthorn, R.C., Sterken, M.G., Pijlman, G.P., Bredenbeek, P.J., and Kieft, J.S. (2018). Mechanism and structural diversity of exoribonuclease-resistant RNA structures in flaviviral RNAs. *Nat. Commun.* 9, 119. <https://doi.org/10.1038/s41467-017-02604-y>.
6. Akiyama, B.M., Eiler, D., and Kieft, J.S. (2016). Structured RNAs that evade or confound exonucleases: function follows form. *Curr. Opin. Struct. Biol.* 36, 40–47. <https://doi.org/10.1016/j.sbi.2015.12.006>.
7. Dreher, T.W. (2010). Viral tRNAs and tRNA-like structures. *Wiley Interdiscip. Rev. RNA* 1, 402–414. <https://doi.org/10.1002/wrna.42>.
8. Geige, R. (1996). Interplay of tRNA-like structures from plant viral RNAs with partners of the translation and replication machineries. *Proc. Natl. Acad. Sci. USA* 93, 12078–12081. <https://doi.org/10.1073/pnas.93.22.12078>.
9. Lu, K., Heng, X., Garyu, L., Monti, S., Garcia, E.L., Kharytonchyk, S., Dorjsuren, B., Kulandaivel, G., Jones, S., Hiremath, A., et al. (2011). NMR detection of structures in the HIV-1 5'-leader RNA that regulate genome packaging. *Science* 334, 242–245. <https://doi.org/10.1126/science.1210460>.
10. Fribe, P., Boudet, J., Simorre, J.P., and Bartenschlager, R. (2005). Kissing-loop interaction in the 3' end of the hepatitis C virus genome essential for RNA replication. *J. Virol.* 79, 380–392. <https://doi.org/10.1128/JVI.79.1.380-392.2005>.
11. Lee, H., Shin, H., Wimmer, E., and Paul, A.V. (2004). cis-acting RNA signals in the NS5B C-terminal coding sequence of the hepatitis C virus genome. *J. Virol.* 78, 10865–10877. <https://doi.org/10.1128/JVI.78.20.10865-10877.2004>.
12. You, S., and Rice, C.M. (2008). 3' RNA elements in hepatitis C virus replication: kissing partners and long poly(U). *J. Virol.* 82, 184–195. <https://doi.org/10.1128/JVI.01796-07>.
13. Goodfellow, I.G., Kerrigan, D., and Evans, D.J. (2003). Structure and function analysis of the poliovirus cis-acting replication element (CRE). *RNA* 9, 124–137. <https://doi.org/10.1261/rna.2950603>.
14. Davis, M., Sagan, S.M., Pezacki, J.P., Evans, D.J., and Simmonds, P. (2008). Bioinformatic and physical characterizations of genome-scale ordered RNA structure in mammalian RNA viruses. *J. Virol.* 82, 11824–11836. <https://doi.org/10.1128/JVI.01078-08>.
15. Simmonds, P., Tuplin, A., and Evans, D.J. (2004). Detection of genome-scale ordered RNA structure (GORS) in genomes of positive-stranded RNA viruses: Implications for virus evolution and host persistence. *RNA* 10, 1337–1351. <https://doi.org/10.1261/rna.7640104>.
16. Plant, E.P., and Dinman, J.D. (2008). The role of programmed-1 ribosomal frameshifting in coronavirus propagation. *Front. Biosci.* 13, 4873–4881. <https://doi.org/10.2741/3046>.
17. Plant, E.P., Pérez-Alvarado, G.C., Jacobs, J.L., Mukhopadhyay, B., Henning, M., and Dinman, J.D. (2005). A three-stemmed mRNA pseudoknot in the SARS coronavirus frameshift signal. *PLoS Biol.* 3, e172. <https://doi.org/10.1371/journal.pbio.0030172>.
18. Siegfried, N.A., Busan, S., Rice, G.M., Nelson, J.A.E., and Weeks, K.M. (2014). RNA motif discovery by SHAPE and mutational profiling (SHAPE-MaP). *Nat. Methods* 11, 959–965. <https://doi.org/10.1038/nmeth.3029>.
19. Zubradt, M., Gupta, P., Persad, S., Lambowitz, A.M., Weissman, J.S., and Rouskin, S. (2017). DMS-MaPseq for genome-wide or targeted RNA structure probing *in vivo*. *Nat. Methods* 14, 75–82. <https://doi.org/10.1038/nmeth.4057>.
20. Mitchell, D., Cotter, J., Saleem, I., and Mustoe, A.M. (2023). Mutation signature filtering enables high-fidelity RNA structure probing at all four nucleobases with DMS. *Nucleic Acids Res.* 51, 8744–8757. <https://doi.org/10.1093/nar/gkad522>.
21. Bohn, P., Gribling-Burrer, A.S., Ambi, U.B., and Smyth, R.P. (2023). Nano-DMS-MaP allows isoform-specific RNA structure determination. *Nat. Methods* 20, 849–859. <https://doi.org/10.1038/s41592-023-01862-7>.
22. Huston, N.C., Wan, H., Strine, M.S., de Cesaris Araujo Tavares, R., Wilen, C.B., and Pyle, A.M. (2021). Comprehensive *in vivo* secondary structure of the SARS-CoV-2 genome reveals novel regulatory motifs and mechanisms. *Mol. Cell* 81, 584–598.e5. <https://doi.org/10.1016/j.molcel.2020.12.041>.
23. Dethoff, E.A., Boerneke, M.A., Gokhale, N.S., Muhire, B.M., Martin, D.P., Sacco, M.T., McFadden, M.J., Weinstein, J.B., Messer, W.B., Horner, S.M., and Weeks, K.M. (2018). Pervasive tertiary structure in the dengue virus RNA genome. *Proc. Natl. Acad. Sci. USA* 115, 11513–11518. <https://doi.org/10.1073/pnas.1716689115>.

24. Wan, H., Adams, R.L., Lindenbach, B.D., and Pyle, A.M. (2022). The In Vivo and In Vitro Architecture of the Hepatitis C Virus RNA Genome Uncovers Functional RNA Secondary and Tertiary Structures. *J. Virol.* 96, e0194621. <https://doi.org/10.1128/jvi.01946-21>.
25. Huston, N.C., Tsao, L.H., Brackney, D.E., and Pyle, A.M. (2024). The West Nile virus genome harbors essential riboregulatory elements with conserved and host-specific functional roles. *Proc. Natl. Acad. Sci. USA* 121, e2312080121. <https://doi.org/10.1073/pnas.2312080121>.
26. Yeh, M.T., Bujaki, E., Dolan, P.T., Smith, M., Wahid, R., Konz, J., Weiner, A.J., Bandyopadhyay, A.S., Van Damme, P., De Coster, I., et al. (2020). Engineering the Live-Attenuated Polio Vaccine to Prevent Reversion to Virulence. *Cell Host Microbe* 27, 736–751.e8. <https://doi.org/10.1016/j.chom.2020.04.003>.
27. Yeh, M.T., Smith, M., Carlyle, S., Konopka-Anstadt, J.L., Burns, C.C., Konz, J., Andino, R., and Macadam, A. (2023). Genetic stabilization of attenuated oral vaccines against poliovirus types 1 and 3. *Nature* 619, 135–142. <https://doi.org/10.1038/s41586-023-06212-3>.
28. Phan, T., Beran, R.K.F., Peters, C., Lorenz, I.C., and Lindenbach, B.D. (2009). Hepatitis C virus NS2 protein contributes to virus particle assembly via opposing epistatic interactions with the E1-E2 glycoprotein and NS3-NS4A enzyme complexes. *J. Virol.* 83, 8379–8395. <https://doi.org/10.1128/JVI.00891-09>.
29. Pirakitkul, N., Kohlway, A., Lindenbach, B.D., and Pyle, A.M. (2016). The Coding Region of the HCV Genome Contains a Network of Regulatory RNA Structures. *Mol. Cell* 62, 111–120. <https://doi.org/10.1016/j.molcel.2016.01.024>.
30. Tuplin, A., Struthers, M., Cook, J., Bentley, K., and Evans, D.J. (2015). Inhibition of HCV translation by disrupting the structure and interactions of the viral CRE and 3' X-tail. *Nucleic Acids Res.* 43, 2914–2926. <https://doi.org/10.1093/nar/gkv142>.
31. Romero-Lopez, C., and Berzal-Herranz, A. (2017). The 5BSL3.2 Functional RNA Domain Connects Distant Regions in the Hepatitis C Virus Genome. *Front. Microbiol.* 8, 2093. <https://doi.org/10.3389/fmicb.2017.02093>.
32. Romero-Lopez, C., and Berzal-Herranz, A. (2009). A long-range RNA-RNA interaction between the 5' and 3' ends of the HCV genome. *RNA* 15, 1740–1752. <https://doi.org/10.1261/rna.1680809>.
33. Hajdin, C.E., Bellaousov, S., Huggins, W., Leonard, C.W., Mathews, D.H., and Weeks, K.M. (2013). Accurate SHAPE-directed RNA secondary structure modeling, including pseudoknots. *Proc. Natl. Acad. Sci. USA* 110, 5498–5503. <https://doi.org/10.1073/pnas.1219988110>.
34. Dorner, K., Ruggeri, C., Zemp, I., and Kutay, U. (2023). Ribosome biogenesis factors—from names to functions. *EMBO J.* 42, e112699. <https://doi.org/10.1525/embj.2022112699>.
35. Juszkiewicz, S., Slodkowicz, G., Lin, Z., Freire-Pritchett, P., Peak-Chew, S.Y., and Hegde, R.S. (2020). Ribosome collisions trigger cis-acting feedback inhibition of translation initiation. *eLife* 9, e60038. <https://doi.org/10.7554/eLife.60038>.
36. Juszkiewicz, S., Speldewinde, S.H., Wan, L., Svejstrup, J.Q., and Hegde, R.S. (2020). The ASC-1 Complex Disassembles Collided Ribosomes. *Mol. Cell* 79, 603–614.e8. <https://doi.org/10.1016/j.molcel.2020.06.006>.
37. Hickey, K.L., Dickson, K., Cogan, J.Z., Replogle, J.M., Schoof, M., D'Orazio, K.N., Sinha, N.K., Hussmann, J.A., Jost, M., Frost, A., et al. (2020). GIGYF2 and 4EHP Inhibit Translation Initiation of Defective Messenger RNAs to Assist Ribosome-Associated Quality Control. *Mol. Cell* 79, 950–962.e6. <https://doi.org/10.1016/j.molcel.2020.07.007>.
38. Gomes-Junior, R., Shigunov, P., Dallagiovanna, B., and Pereira, I.T. (2022). Assessing the Human Pluripotent Stem Cell Translatome by Polyosome Profiling. *Methods Mol. Biol.* 2520, 309–319. https://doi.org/10.1007/978-1-4939-3591-8_11.
39. Kudla, M., and Karginov, F.V. (2016). Measuring mRNA Translation by Polysome Profiling. *Methods Mol. Biol.* 1421, 127–135. https://doi.org/10.1007/978-1-4939-3591-8_11.
40. Schult, P., Roth, H., Adams, R.L., Mas, C., Imbert, L., Orlik, C., Ruggieri, A., Pyle, A.M., and Lohmann, V. (2018). microRNA-122 amplifies hepatitis C virus translation by shaping the structure of the internal ribosomal entry site. *Nat. Commun.* 9, 2613. <https://doi.org/10.1038/s41467-018-05053-3>.
41. Rampasek, L., Jimenez, R.M., Luptak, A., Vinar, T., and Brejova, B. (2016). RNA motif search with data-driven element ordering. *BMC Bioinf.* 17, 216. <https://doi.org/10.1186/s12859-016-1074-x>.
42. Bellaousov, S., and Mathews, D.H. (2010). ProbKnot: fast prediction of RNA secondary structure including pseudoknots. *RNA* 16, 1870–1880. <https://doi.org/10.1261/rna.2125310>.
43. Yu, Y., Wan, Z., Wang, J.H., Yang, X., and Zhang, C. (2022). Review of human pegiviruses: Prevalence, transmission, pathogenesis, and clinical implication. *Virulence* 13, 324–341. <https://doi.org/10.1080/21505594.2022.2029328>.
44. Masaki, T., Arend, K.C., Li, Y., Yamane, D., McGivern, D.R., Kato, T., Wakita, T., Moorman, N.J., and Lemon, S.M. (2015). miR-122 stimulates hepatitis C virus RNA synthesis by altering the balance of viral RNAs engaged in replication versus translation. *Cell Host Microbe* 17, 217–228. <https://doi.org/10.1016/j.chom.2014.12.014>.
45. Gamarnik, A.V., and Andino, R. (1998). Switch from translation to RNA replication in a positive-stranded RNA virus. *Genes Dev.* 12, 2293–2304. <https://doi.org/10.1101/gad.12.15.2293>.
46. Chen, J., Noueiry, A., and Ahlquist, P. (2001). Brome mosaic virus Protein 1a recruits viral RNA2 to RNA replication through a 5' proximal RNA2 signal. *J. Virol.* 75, 3207–3219. <https://doi.org/10.1128/JVI.75.7.3207-3219.2001>.
47. Noueiry, A.O., and Ahlquist, P. (2003). Brome mosaic virus RNA replication: revealing the role of the host in RNA virus replication. *Annu. Rev. Phytopathol.* 41, 77–98. <https://doi.org/10.1146/annurev.phyto.41.052002.095717>.
48. Khan, D., and Fox, P.L. (2024). Host-like RNA Elements Regulate Virus Translation. *Viruses* 16, 468. <https://doi.org/10.3390/v16030468>.
49. Richter, J.D., and Coller, J. (2015). Pausing on Polyribosomes: Make Way for Elongation in Translational Control. *Cell* 163, 292–300. <https://doi.org/10.1016/j.cell.2015.09.041>.
50. Leppek, K., Byeon, G.W., Kladwang, W., Wayment-Steele, H.K., Kerr, C.H., Xu, A.F., Kim, D.S., Topkar, V.V., Choe, C., Rothschild, D., et al. (2022). Combinatorial optimization of mRNA structure, stability, and translation for RNA-based therapeutics. *Nat. Commun.* 13, 1536. <https://doi.org/10.1038/s41467-022-28776-w>.
51. Chillon, I., Marcia, M., Legiewicz, M., Liu, F., Somarowthu, S., and Pyle, A.M. (2015). Native Purification and Analysis of Long RNAs. *Methods Enzymol.* 558, 3–37. <https://doi.org/10.1016/bs.mie.2015.01.008>.
52. Kazakov, T., Yang, F., Ramanathan, H.N., Kohlway, A., Diamond, M.S., and Lindenbach, B.D. (2015). Hepatitis C virus RNA replication depends on specific cis- and trans-acting activities of viral nonstructural proteins. *PLoS Pathog.* 11, e1004817. <https://doi.org/10.1371/journal.ppat.1004817>.
53. Feigelstock, D.A., Mihalik, K.B., Kaplan, G., and Feinstone, S.M. (2010). Increased susceptibility of Huh7 cells to HCV replication does not require mutations in RIG-I. *Virol. J.* 7, 44. <https://doi.org/10.1186/1743-422X-7-44>.
54. Tang, G.Q., Nandakumar, D., Bandwar, R.P., Lee, K.S., Roy, R., Ha, T., and Patel, S.S. (2014). Relaxed rotational and scrunching changes in P266L mutant of T7 RNA polymerase reduce short abortive RNAs while delaying transition into elongation. *PLoS One* 9, e91859. <https://doi.org/10.1371/journal.pone.0091859>.
55. Busan, S., and Weeks, K.M. (2018). Accurate detection of chemical modifications in RNA by mutational profiling (MaP) with ShapeMapper 2. *RNA* 24, 143–148. <https://doi.org/10.1261/rna.061945.117>.

56. Minskaia, E., and Ryan, M.D. (2013). Protein coexpression using FMDV 2A: effect of “linker” residues. *BioMed Res. Int.* 2013, 291730. <https://doi.org/10.1155/2013/291730>.
57. Ananthanarayanan Kumar, H.W., Perry, Z., Patel, S., Tavares, R., and Marie Pyle, A. (2023). Discovery of a Well-Folded Protein Interaction Hub Within the Human Long Non-Coding RNA NORAD. Preprint at bioRxiv. <https://doi.org/10.1101/2023.08.07.552337>.
58. Hughes, C.S., Moggridge, S., Müller, T., Sorensen, P.H., Morin, G.B., and Krijgsveld, J. (2019). Single-pot, solid-phase-enhanced sample preparation for proteomics experiments. *Nat. Protoc.* 14, 68–85. <https://doi.org/10.1038/s41596-018-0082-x>.
59. Searle, B.C., Pino, L.K., Egertson, J.D., Ting, Y.S., Lawrence, R.T., MacLean, B.X., Villén, J., and MacCoss, M.J. (2018). Chromatogram libraries improve peptide detection and quantification by data independent acquisition mass spectrometry. *Nat. Commun.* 9, 5128. <https://doi.org/10.1038/s41467-018-07454-w>.
60. Graw, S., Tang, J., Zafar, M.K., Byrd, A.K., Bolden, C., Peterson, E.C., and Byrum, S.D. (2020). proteinNorm - A User-Friendly Tool for Normalization and Analysis of TMT and Label-Free Protein Quantification. *ACS Omega* 5, 25625–25633. <https://doi.org/10.1021/acsomega.0c02564>.
61. Ritchie, M.E., Phipson, B., Wu, D., Hu, Y., Law, C.W., Shi, W., and Smyth, G.K. (2015). limma powers differential expression analyses for RNA-seq and microarray studies. *Nucleic Acids Res.* 43, e47. <https://doi.org/10.1093/nar/gkv007>.

STAR★METHODS

KEY RESOURCES TABLE

REAGENT or RESOURCE	SOURCE	IDENTIFIER
Antibodies		
RPL14 antibody	proteintech	14991-1-AP; RRID: AB_2285319
RPL9 antibody	abcam	ab182556
ZNF598 antibody	Bethyl Laboratories	A305-108A-T; RRID: AB_2631503
GIGYF2 antibody	proteintech	24790-1-AP; RRID: AB_2879727
Goat anti-Rabbit IgG, Alexa Fluor™ Plus 555	Thermo Fisher	A32732; RRID: AB_2633281
Goat anti-Mouse IgG, Cyanine5	Thermo Fisher	A10524; RRID: AB_10562712
Bacterial and virus strains		
Hepatitis C virus (HCV) Jc1	Phan et al. ²⁸	derived from GenBank: JF343782.1
Chemicals, peptides, and recombinant proteins		
DPBS	ThermoFisher	14190144
NAI	MilliporeSigma	03-310
DMSO	Sigma-Aldrich	276855-100mL
Trizol	ThermoFisher	15596018
Chloroform:Isoamyl alcohol 24:1	MilliporeSigma	C0459-1PT
AmpureXP beads	Beckman coulter	A63880
Puromycin Dihydrochloride	ThermoFisher	A1113803
Cycloheximide solution	Sigma	C4859
Experimental models: Cell lines		
Huh7.5 cells	Phan et al. ²⁸	N/A
Huh7.5 cells with stable expression of HCV SGR	Phan et al. ²⁸	N/A
Oligonucleotides		
RT, PCR and qPCR primer, LNA	This paper	Table S1
Software and algorithms		
ShapeMapper2	Busan et al. ⁵¹	https://github.com/Weeks-UNC/shapemapper2
ShapeKnots	Hajdin et al. ³³	https://rna.urmc.rochester.edu/RNAstructure.html
SuperFold	Siegfried et al. ¹⁸	https://weekslab.com/software/

EXPERIMENTAL MODEL AND STUDY PARTICIPANT DETAILS

The Huh7.5 cell line and Huh7.5 cells constitutively expressing the HCV subgenomic replicon⁵² (Huh7.5-SGR) were gifts from Dr. Brett Lindenbach (Yale University). These cells are known to harbor the RIG-I (DDX58) mutation (Thr551le).⁵³ We did not perform independent STR profiling for authentication. Huh7.5 cells were maintained in Dulbecco's Modified Eagle Medium (Genesee 25–501) supplemented with 10% fetal bovine serum (Genesee 25-550H) and nonessential amino acids (Thermo Fisher 11140050). Huh7.5-SGR cells were cultured under the same conditions, with the addition of 1 mg/mL G418 (ALX-380-013-G005). All Cell lines were tested for mycoplasma contamination using a PCR-based assay and were confirmed to be negative. All experiments involving live HCV were performed in a BSL-2+ facility in Dr. Lindenbach's lab.

METHOD DETAILS

Construct design and preparation

All constructs used in this study were cloned via Gibson assembly. The insert and backbone were amplified using Q5 Hot Start polymerase (NEB M0491S) and purified with Monarch DNA Cleanup Kits (NEB T1030S). Gibson assembly was carried out using NEB Gibson Assembly Master Mix (E2611S) following the manufacturer's protocol. The sequences of the cloned constructs were verified by whole-plasmid sequencing at Quintara Biosciences. Plasmids were purified using the Qiagen Maxi Prep Kit (#12263), and their sequences are available in the [supplemental information](#).

For all luciferase constructs containing pseudoknot1 (pk1), in silico RNA structure predictions were performed using Superfold¹⁸ to ensure no strong interactions (base-pair probability >80%) occurred between pk1 and adjacent luciferase or linker sequence. Linker sequences and lengths were adjusted to meet this criterion.

Pk1 RNA *in vitro* transcription, folding, and SHAPE modification

The HCV-pk1 plasmid was linearized using EcoRI (NEB) and the HCV-pk1 RNA was *in vitro* transcribed by runoff transcription with T7 RNA polymerase P266L variant⁵⁴ under the following buffer condition: 120mM MgCl₂, 400mM Tris-HCl [pH 8.0], 20mM Spermidine, 100mM NaCl, 0.1% Triton X-100, at 37°C for 2hours.⁵¹ Following transcription, RQ1 DNase (Promega M6101) was used to digest the plasmid template at 37°C for 20 min, and 25 mM EDTA (pH 8.0) was added to chelate Mg²⁺. Size-exclusion chromatography was performed at room temperature using Superdex 200 10/300 GL (24 mL), equilibrated with filtration buffer (50 mM K- HEPES [pH 7.5], 150 mM KCl, and 100 mM EDTA). RNA from the peak fraction was diluted to 100 ng/uL and folded by incubating with the desired concentration of MgCl₂ at 37°C for 30 min. SHAPE modification was performed by adding a final concentration of 200 mM NAI (Sigma 03-310) or the same volume of DMSO and incubated at 37°C for 10 min. RNA was then precipitated using 300mM NaOAc and 80% EtOH, washed once with 80% EtOH, and resuspended in RNA storage buffer (10 mM MOPS [pH 6.0] and 1 mM EDTA).

Reverse transcription, library preparation and data analysis for *in vitro* SHAPE-MaP

In vitro-purified RNA (0.5ug) was reverse transcribed using 200 U SuperScript II (Thermo Fisher 18064014) with 1pmol gene specific primer under standard buffer conditions (50 mM Tris-HCl [pH 8.3], 75 mM KCl, 10 mM DTT, 6 mM MnCl₂, and 0.5 mM dNTP mix). cDNA was cleaned up using AMPure XP beads (Beckman A63881) and amplified with Q5 Hot Start polymerase (NEB M0491S). RT and PCR primer are provided in [supplemental information](#). The PCR product was then purified with Monarch DNA cleanup kits (NEB T1030S) and diluted to 0.2 ng/uL. Sequencing libraries were prepared using the Nextera XT DNA library preparation kit (Illumina), following the manufacturer's protocol. Library quantification was performed using a Qubit fluorometer (Life Technologies) and Agilent Bioanalyzer. Sequencing was carried out on the NextSeq 2000 system (Illumina). SHAPE-MaP libraries were analyzed with ShapeMapper 2⁵⁵ software, and all libraries successfully met the three quality-control criteria of ShapeMapper 2.

Full-length HCV growth luciferase assay

The HCV luciferase reporter construct was a gift from Dr. Brett Lindenbach (Yale University), it is based on HCV genotype Jc1 (derived from GenBank: JF343782.1), the full-length sequence is provided in [supplemental information](#). A Gaussia princeps luciferase (Gluc) reporter is inserted between the viral p7 and NS2 proteins, adjacent to a Foot-and-mouth disease virus (FMDV) 2A "autocleaving peptide"⁵⁶ for Gluc release, providing a quantitative measure of HCV replication.^{28,29}

The full-length HCV template plasmid was linearized using XbaI (NEB), *in vitro* transcribed as described above. Following transcription, the plasmid template was digested with RQ1 DNase (Promega M6101), and the RNA was purified using the RNeasy kit (Qiagen 74104) according to the manufacturer's protocol. The RNA was eluted in RNA storage buffer at a final concentration of 1 µg/uL. The purified RNA was run on a 1% denaturing agarose gel to confirm the RNA's size and integrity.

Luciferase assays were performed in a 12-well plate format. Huh7.5 cells were plated at 2×10^5 cells/mL. ~16h post plating, 1ug of HCV RNA or mutant was transfected per well using the Mirus mRNA transfection reagent (MIR-2250) according to the manufacturer's protocol. For experiments involving locked nucleic acids (LNAs), 0.48nmol LNA was co-transfected with 1ug HCV RNA using the MIR-2250 mRNA transfection reagent. At each designated time point, the medium was collected, and cells were washed once with phosphate-buffered saline (PBS), followed by the addition of fresh medium. The collected medium was clarified by centrifugation (5 min at 20,000 g), transfer to fresh tubes, mixed with an equal volume of 2× luciferase lysis buffer, and stored at -20°C. Luminescence was measured using a Bitek Synergy H1 plate reader by adding 50 µL of Gaussia luciferase reagent (Pierce Gaussia luciferase flash assay kit; Thermo Fisher 16159) to 20 µL of the medium with a 5-s integration time.

LNAs were designed with three consecutive LNA bases at both the 5' and 3' ends of each oligo-nucleotide, with stretches of un-locked bases limited to three consecutive nucleotides.²² All LNAs were designed with similar length, %GC content, %LNA content, and LNA:RNA duplex Tm. The sequence of the LNAs were provided in [supplemental information](#).

In vitro RNP pull-down

RNA preparation

All RNA constructs were *in vitro* transcribed and purified using size-exclusion chromatography as described above. RNA from the peak fraction was diluted to 2uM and folded by incubation with 10mM Mg²⁺ at 37°C for 30 min.

Whole-cell lysate preparation

Huh7.5-SGR cells (20 million) were resuspended in 500ul of cold BufferA (10mM HEPES [pH7.5], 1.5mM MgCl₂, 10mM KCl, 0.5mM DTT, 1X protease inhibitor, 0.1U/uL RNase inhibitor, 8mM Ribonucleoside vanadyl complexes) and incubated on ice for 10 min. The cell suspension was homogenized by passing through a cell homogenizer 20 times. The lysate was then clarified by centrifugation at 20,000g for 10 min at 4°C. The supernatant was transferred to a fresh tube, and MgCl₂ and KCl were added to final concentrations of 10 mM and 150 mM, respectively.

Pull-down experiment

For each sample, 25 µL of Amylose resin (NEB E8021S) was prepared by washing with 1 mL of water and 1 mL of Amylose wash buffer (20 mM HEPES [pH 7.0], 100 mM KCl, 10 mM MgCl₂, 1 mM TCEP, 0.01% Tween, 0.2% NP-40, 1× protease inhibitor, 0.1 U/µL RNase inhibitor). The resin was resuspended in 0.5 mL of Amylose wash buffer, and the purified MBP-MS2 fusion protein (as described in Kumar et al.,⁵⁷) was added to a final concentration of 1 µM. The binding reaction was performed by rotating the mixture at 4°C for 1 h. Excess MBP-MS2 protein was removed by centrifugation at 600g for 1 min, followed by two washes with Amylose wash buffer. The resin was then resuspended with 0.5 mL of 2 µM folded RNA and incubated at room temperature for 30 min with rotation. Unbound RNA was removed by centrifugation at 600g for 1 min, followed by two washes with Amylose wash buffer. At this stage, the resin was loaded with the MBP-MS2-RNA complex.

Next, the resin was resuspended with 500 µL of total cell extract from HuH7.5-SGR cells (from 20 million cells), and protein pull-down was performed by incubating the mixture at 4°C for 1 h with rotation. Unbound proteins were removed by centrifugation at 600g for 1 min, followed by two washes with Amylose wash buffer. The bound proteins were eluted by incubating the resin with 30 µL of Amylose elution buffer (20 mM HEPES [pH 7.0], 100 mM KCl, 10 mM MgCl₂, 1 mM TCEP, 0.01% Tween, 10 mM Maltose) on ice for 15 min.

A small aliquot of the eluted sample was analyzed on a 6% denaturing RNA gel and a 4%-12% NuPAGE gel (Thermo Fisher NP0329BOX) to confirm the sizes of the bait RNA and MBP-MS2 fusion protein. The NuPAGE gel was stained with SyproRuby (Thermo Fisher S12000) and destained using a 50% methanol, 10% acetic acid solution. The remaining eluted samples were flash-frozen in liquid nitrogen and stored at -80°C for subsequent mass spectrometry analysis.

Mass spectrometry and data analysis

Mass spectrometry experiments and data analysis were conducted by the IDeA National Resource for Quantitative Proteomics. A full list of protein hits is provided in the [supplemental information](#).

Protein samples were reduced, alkylated, and digested using single-pot, solid-phase-enhanced sample preparation⁵⁸ with sequencing grade modified porcine trypsin (Promega). Tryptic peptides were then separated by reverse phase XSelect CSH C18 2.5 µm resin (Waters) on an in-line 150 × 0.075 mm column using an UltiMate 3000 RSLC nano system (Thermo). Peptides were eluted using a 60 min gradient from 98:2 to 65:35 buffer A:B ratio. Eluted peptides were ionized by electrospray (2.2 kV) followed by mass spectrometric analysis on an Orbitrap Exploris 480 mass spectrometer (Thermo). To assemble a chromatogram library, six gas-phase fractions were acquired on the Orbitrap Exploris with 4 m/z DIA spectra (4 m/z precursor isolation windows at 30,000 resolution, normalized AGC target 100%, maximum inject time 66 ms) using a staggered window pattern from narrow mass ranges using optimized window placements. Precursor spectra were acquired after each DIA duty cycle, spanning the m/z range of the gas-phase fraction (i.e., 496–602 m/z, 60,000 resolution, normalized AGC target 100%, maximum injection time 50 ms). For wide-window acquisitions, the Orbitrap Exploris was configured to acquire a precursor scan (385–1015 m/z, 60,000 resolution, normalized AGC target 100%, maximum injection time 50 ms) followed by 50 × 12 m/z DIA spectra (12 m/z precursor isolation windows at 15,000 resolution, normalized AGC target 100%, maximum injection time 33 ms) using a staggered window pattern with optimized window placements. Precursor spectra were acquired after each DIA duty cycle.

Following data acquisition, data were searched using an empirically corrected library against the UniProt Homo sapiens database (January 2023) and HCV proteins (Uniport ID: Q99IB8, A3EZI9, D2K2A7, Q1I054, O39474, O39930). A quantitative analysis was performed to obtain a comprehensive proteomic profile. Proteins were identified and quantified using EncyclopeDIA⁵⁹ and visualized with Scaffold DIA using 1% false discovery thresholds at both the protein and peptide level. Protein MS2 exclusive intensity values were assessed for quality using ProteiNorm.⁶⁰ The data was normalized using Cyclic Loess⁶¹ and analyzed using proteoDA to perform statistical analysis using Linear Models for Microarray Data (limma) with empirical Bayes (eBayes) smoothing to the standard errors.⁶¹ Proteins with an FDR adjusted p-value <0.05 and a fold change >2 were considered significant.

Western Blot

Protein samples were mixed with 2X SDS loading dye and boiled at 95°C before running on NuPAGE Novex 4–12% Bis-Tris Protein Gels (Thermo Fisher). The proteins on the gel were transferred using wet transfer system to 0.45 µm PVDF membrane (Sigma IPVH00010) at 100V for 1.5 h. The membrane was blocked using 5% milk in TBST buffer (20 mM Tris [pH 7.4], 150 mM NaCl, 0.05% Tween) at room temperature for 1 h and then blotted with first antibody at desired concentration for 16 hours at 4°C. anti RPL9 (abcam ab182556) was used at 1:250 dilution; anti RPL14 (proteintech 14991-1-AP) was used at 1:500 dilution; anti ZNF598 (Bethyl Laboratories A305-108A-T) was used at 1:1000 dilution; anti GIGYF2 (proteintech 24790-1-AP) was used at 1:1000 dilution. Fluorescent mouse/rabbit secondary antibody (Thermo Fisher A10524, A32732) were used at 1:25000 dilution in TBST and incubated 1 h at room temperature avoiding light. All blots were visualized using Typhoon scanner.

Visualizing pk1 binding with ribosome using negative stain

The pull-down was performed as described in the “*in vitro* RNP pull down” section, with modifications. Specifically, 200 µL of Rabbit reticulocyte lysate (Promega L4540) was used, spiked with 5 mM MgCl₂ and 100 mM KCl. The elution sample was diluted to 0.1 mg/mL and 4 µL was loaded onto negative stain grids (CF300-Cu-50) and screened on Talos 120 KV.

Translation luciferase assay

The translation luciferase constructs were linearized using EcoRI, *in vitro* transcribed as described above. Following transcription, the plasmid template was digested with RQ1 DNase (Promega M6101), and the RNA was purified using the RNeasy kit (Qiagen 74104) according to the manufacturer's protocol. The RNA was eluted in RNA storage buffer at a final concentration of 1 µg/µL. The quality and size of the purified RNA were verified by running it on a 1% denaturing agarose gel.

If a type-I cap was required for translation initiation, the RNA was capped using Vaccinia Capping Enzyme (NEB M2080S) and 2'-OMe transferase (NEB M0366S) following the manufacturer's protocols. After capping, the RNA was purified again using the RNeasy kit and eluted in RNA storage buffer at a final concentration of 1 µg/µL.

For the luciferase assay, Huh7.5 cells were plated in 12-well plates at a density of 2×10^5 cells/mL. Approximately 16 h post-plating, 1 µg of RNA construct was transfected per well using the Mirus mRNA lipid transfection reagent (MIR-2250) according to the manufacturer's protocol. All timepoints reported in the paper indicate the time after this step. At each time point, the medium was collected, cells were washed once with phosphate-buffered saline (PBS), and fresh medium was added. The collected medium was clarified by centrifugation at 20,000 × g for 5 min. Luminescence was measured using a Biotek Synergy H1 plate reader with 20 µL of medium, 50 µL of 10 µM Gaussia luciferase substrate Coelenterazine (Promega S2001), and a 5-s integration time.

Translation dual luciferase assay

RNA preparation and transfection were conducted as described for the single translation luciferase assay. Two hours post-transfection, the cells were lysed, and luciferase activity was measured using the Dual-Luciferase Reporter Assay System (Promega E1960) according to the manufacturer's instructions. Luminescence was assessed on a Biotek Synergy H1 plate reader with 20 µL of cell lysate and 50 µL each of Gaussia and Firefly luciferase reagents.

siRNA knockdown

1×10^5 Huh7.5 cells were plated in 12 well plate approximately 16 h before transfection. On the day of transfection, 28 pmol of siRNA per well targeting GIGYF2 (Thermo Fisher s25033), ZNF598 (Thermo Fisher s40509), or a control siRNA (Thermo Fisher 4390843) were transfected into the cells using TransIT-siQUEST (Mirus 2114) according to the manufacturer's instructions. 72 h post-siRNA transfection, cells were used for the dual luciferase assay.

Polysome profiling experiment

3×10^6 Huh7.5 cells were plated in a 10 cm dish and transfected with 15.5 µg of full-length HCV RNA or mutant RNA using Mirus mRNA lipid transfection reagent (MIR-2250) according to the manufacturer's protocol. At 70 h post-transfection, cells treated with Puromycin control were incubated with 50 µg/mL Puromycin for 2 h. To compare translational states under different conditions, cells from Puromycin and HCV-untreated cells were prepared in parallel. At 72 h post-transfection, cells were washed with PBS and incubated with medium containing 100 µg/mL cycloheximide for 10 min. The cells were then washed three times with PBS containing 100 µg/mL cycloheximide and harvested with a cell scraper. For each plate, cells were lysed with 1 mL of polysome lysis buffer (15 mM Tris [pH 7.5], 5 mM MgCl₂, 150 mM NaCl, 2 mM DTT, 100 µg/mL cycloheximide, 1% Triton X-100, 1X protease inhibitor) by mixing and incubated at 4°C for 5 min. The lysate was then cleared by centrifugation at 20,000 × g for 10 min.

The cleared lysate was separated on a linear 10%–50% sucrose gradient (15 mM Tris pH 7.5, 5 mM MgCl₂, 150 mM NaCl, 2 mM DTT, 100 µg/mL cycloheximide) which were made and fractionated using Biocomp Gradient Station (Biocomp instruments). Gradients were centrifuged at 36,000 RPM at 4C in a Beckmann SW41 rotor for 2 h. Absorbances were monitored at 260 nm during fractionation.

RNA was extracted from each fraction using TRIzol reagent (Thermo Fisher 15596018) and purified using Zymo RNA Clean & Concentrator (R1016). cDNA was synthesized using random hexamers and SSIII (Thermo Fisher 18-080-044) following the manufacturer's protocols. Quantitative PCR (qPCR) was performed with SYBR Green qPCR Mastermix (Roche 50-720-3180) using gene-specific primers for HCV and Actin. Primer sequences are provided in the [supplemental information](#).

A standard curve was generated using serially diluted *in vitro* transcribed HCV and Actin RNA. RNA copy numbers in each fraction were calculated using linear regression derived from the standard curve and normalized to the total RNA amount input (copies/µg of total RNA). The RNA distribution across each fraction was determined by normalizing the RNA copy number in each fraction to the total RNA copy number across all fractions.

In silico structure prediction pipeline

RNA virus genome sequences were downloaded from the NCBI Virus Genome Database (RefSeq, June 2024). Structure homology searches were conducted using RNARobo⁴¹ with the option to report non-overlapping structures. The descriptor file is provided in [Figure S2](#). The output from RNARobo is used for in-silico structure prediction using SHAPEKnots⁴² (implemented in RNAstructure) with default parameters. The results from SHAPEKnots were manually examined to confirm the prediction of pseudoknot-like structures.

Subsequently, surrounding structure predictions were performed using SHAPEKnots by applying a sliding window approach: five windows of approximately 300 nucleotides each, with 50-nucleotide steps, were used to cover the pseudoknot region. Using HCV-pk1 as a benchmark, we setup the passing criteria as: a pk1-like structure was considered valid if it is observed in at least one window in one of the low free energy predictions.

QUANTIFICATION AND STATISTICAL ANALYSIS

For the plots in [Figure 2B](#) and [Figure S1C](#), statistical analysis was performed using Linear Models for Microarray Data (limma) with empirical Bayes (eBayes) smoothing of the standard errors. Proteins with an FDR-adjusted p -value <0.05 and a fold change >2 were considered significant. Statistical analyses for all other figures were performed in GraphPad Prism 9 using unpaired t tests with equal variance assumed. All bar plots are presented as means, with standard deviation shown as error bars. Significance of comparisons is indicated in figures and supplemental figures as *, $p < 0.05$; **, $p < 0.01$; ***, $p < 0.001$; ****, $p < 0.0001$.